Research Article

Enhancing Performance and Security of IRS-NOMA Systems with Multiple Eavesdroppers and Hardware Impairments

Phu Tran TIN[1], *Minh-Sang Van NGUYEN*[2], *Tran Trung DUY*[2,*], *Quy-Anh BUI*[1], *Byung-Seo KIM*[3], *Lubos REJFEK*[4]

[1]Data Science Laboratory, Faculty of Information Technology, Ton Duc Thang University, Ho Chi Minh City, Vietnam
[2]Faculty of Telecommunications 2, Posts and Telecommunications Institute of Technology, Ho Chi Minh City, Vietnam
[3]Department of Software and Communications Engineering, Hongik University, Sejong 30016, South Korea
[4]Faculty of Electrical Engineering and Informatics, University of Pardubice, nám. Čsl. Legií 595, Pardubice 530 02, Czech Republic

phutrantin@tdtu.edu.vn, sangnvm@ptit.edu.vn, duytt@ptit.edu.vn, buiquyanh@tdtu.edu.vn, jsnbs@hongik.ac.kr, lubos.rejfek@upce.cz

[*]Corresponding author: Tran Trung Duy; duytt@ptit.edu.vn

DOI: 10.15598/aeee.v24ix.251020

Article history: Received Oct 28, 2025; Revised Dec 16, 2025; Accepted Feb 01, 2026; First Published May 13, 2026.

Abstract. *This article examines the integration of non-orthogonal multiple access (NOMA) with intelligent reconfigurable surfaces (IRS). It focuses on addressing these challenges while mitigating the adverse effects of residual hardware impairments (RHI), which cause signal distortion. The primary contribution of this paper lies in deriving precise closed-form expressions for both connection outage probability (COP) and intercept probability (IP) within the proposed system. Additionally, a Deep Neural Network (DNN) model was developed to estimate COP and IP, complemented by Monte Carlo simulations to validate analytical results. Simulation findings reveal clear quantitative performance gains. For instance, increasing IRS reflecting elements from 10 to 30 reduces the COP by 18% at a signal-to-noise ratio (SNR) of 20 dB. Similarly, increasing the amplitude reflection coefficient from 0.4 to 0.9 results in a 30% IP reduction. Increasing the number of eavesdroppers (Es) from 1 to 5 yields an IP reduction of 8% at an SNR of 15 dB. Similarly, lowering the hardware-impairment coefficient from 0.02 to 0.03 improves the COP by 17% at an SNR of 20 dB, while the IP decreases by 4% under the same conditions. Moreover, increasing the power allocation of the user from 0.2 to 0.3 yields a COP reduction of 4% at an SNR of 17 dB, while the IP decreases by 4% under the same conditions. Overall, the proposed IRS-assisted NOMA architecture demonstrates substantial resilience and security improvements for Internet of Things (IoT) networks affected by hardware imperfections.*

Keywords

Hardware Impairments, Intelligent Reflecting Surface, Non-Orthogonal Multiple Access, Physical Layer Security.

1. Introduction

In recent years, there has been a notable surge in the development of new wireless communication frameworks in both academia and industry. The primary drivers of this increased focus are the expanding need for secure communication and higher data

transfer rates. Moreover, the demand for more connections extends beyond fifth-generation (B5G) and sixth-generation (6G) networks [1–3]. The widespread usage of the Internet of Things (IoT) devices across a range of applications, from smart homes to healthcare and industrial automation, has further exacerbated this demand. Thus, there is an urgent need for robust communication infrastructures that provide security and reliability [4,5]. The focus on physical layer security (PLS) is essential since wireless communication is broadcast by nature, which leaves transmitted data vulnerable to eavesdropping.

1.1. Related works

Among emerging technologies, the reconfigurable intelligent surface (RIS) stands out among new technologies due to its capacity to revolutionize wireless networks. These technologies are characterized by low power consumption, cost-effectiveness, and simplicity of deployment. Furthermore, their sophisticated adaptive beamforming and smart channel modeling capabilities are key reasons for their adoption [1,6,7]. RIS dynamically optimizes the propagation environment to provide dependable and secure communication in IoT systems, addressing issues like device heterogeneity and dense deployments. RIS is the ideal technology for secure communications due to its ability to establish regulated transmission environments. In particular, the RIS technology uses its unique qualities by strengthening signals for authorized users while weakening signals captured by possible eavesdroppers (Es). This reconfiguration establishes a virtual line-of-sight (LoS) link and compensates for long-distance power loss. Furthermore, it ensures secure data transmission by optimizing reflection coefficients [8,9]. RIS and non-orthogonal multiple access (NOMA) present significant advantages in addressing the security and privacy protection requirements of future network infrastructures. A scheme for intelligent reconfigurable surfaces (IRS)-assisted secure communication was proposed in [10,11]. This approach enhances transmission reliability while satisfying concealment constraints. It was verified that the IRS-NOMA network outperforms the IRS-assisted orthogonal multiple access (OMA) network in terms of secrecy outage probability (SOP) [12–14]. The covert communication performance of the RIS-NOMA network was investigated in [15], which showed that the use of NOMA and IRS can improve the performance of covert communication.

PLS has emerged as an effective approach for safeguarding wireless communication against eavesdropping without relying on conventional cryptographic techniques. In [16], the authors investigated a downlink RIS-assisted short-packet NOMA system, focusing on enhancing the security of the user-pairing process in the presence of untrusted users. The work in [17] analyzed the effective secrecy capacity (ESC) of an RIS-assisted NOMA network under delay constraints, where ESC was employed as a key metric to capture the impact of latency on secure communication performance. In [18], robust transmission design for an RIS-aided secure communication system subject to transceiver hardware impairments (HIs) was studied, to maximize the secrecy rate while satisfying both the base station (BS) transmit power constraint and the RIS unit-modulus reflection constraint. Similarly, [19] proposed a robust transmission scheme for RIS-aided NOMA secure networks considering transceiver HIs, under two eavesdropping scenarios and two artificial noise generation strategies. Furthermore, the work in [20] examined RIS-assisted secure multi-user communication in the presence of HIs at both the RIS and transceivers, wherein the beamforming vectors at the BS and the RIS phase shifts were jointly optimized to maximize the weighted minimum approximate ergodic secrecy rate under the BS power and RIS unit-modulus constraints. However, despite these significant efforts, several important issues remain unaddressed. First, most existing works consider either ideal hardware conditions, a limited number of Es, or simplified models. Second, prior studies primarily focus on secrecy rate or ESC analysis. At the same time, the joint evaluation of both reliability and security through connection outage probability (COP) and intercept probability (IP) has received insufficient attention, particularly in the presence of multiple passive Es. Third, none of the aforementioned works incorporate learning-based approaches to predict COP and IP, even though analytical expressions become highly complex or intractable under hardware and multi-eavesdropper settings. These limitations motivate the need for a comprehensive framework that simultaneously considers IRS-assisted NOMA transmission, HIs, multiple Es, and data-driven performance prediction.

In recent years, deep learning (DL) has increasingly attracted the attention of researchers in the communications field due to its ability to predict performance metrics of analytically complex networks with low computational complexity [21,22]. DL is adept at discerning intricate patterns and relationships within data, making it suitable for performance analysis. Within this framework, deep neural networks (DNNs) can be trained using historical outage and capacity data, network performance metrics, and other system parameters to achieve precise modeling and prediction of outage probability (OP) and ergodic capacity [21]. By processing extensive datasets, DNNs uncover complex patterns and relationships that traditional analytical methods often overlook, resulting in enhanced accuracy and expedited performance predictions. Furthermore, a DNN-based approach was implemented to enhance uplink NOMA security combined with IRS by

predicting system performance as OP and system security through IP [23].

1.2. Motivation and Contributions

In [24], the downlink system model with two users via IRS was examined, taking into account the impact of HIs on this model. Additionally, this study examined the impact of HIs on all devices and assessed several system performances, including OP. Unfortunately, this study did not address the incorporation of many Es into the eavesdropping system from the BS or an examination of the system's security through the use of IP analysis. Furthermore, it didn't take into account employing a DNN to forecast the best performance results. In [25], the authors investigated a downlink IRS-NOMA network model, with particular attention to the effects of HIs. The study further analyzed system performance by evaluating OP and throughput. In addition, it did not address the presence of multiple Es, and consequently, the system's security performance in terms of IP was not assessed. Additionally, the research did not explore predicting system performance through the application of DNNs. In [26], the authors investigated the downlink secure network model with multiple eavesdropping devices and evaluated its security performance. However, this study did not consider the integration of IRS into the system model, nor did it analyze the system reliability through COP or the security capability through IP. In addition, the integration of a DNN to predict the optimal system performance was also not addressed.

Motivated by the aforementioned research gaps, this paper investigates a secure downlink cooperative NOMA network integrated with an IRS in the presence of multiple Es. Moreover, a DNN is incorporated into the system model to predict system performance outcomes. This approach can serve as a case study for evaluating and forecasting system performance in practical deployment scenarios. The main contributions of this work can be succinctly articulated as follows:

- Unified IRS–NOMA PLS framework with practical impairments: This paper investigates a downlink IRS-aided NOMA network in the presence of multiple passive Es, explicitly incorporating residual HIs at all transceivers, namely the BS, legitimate users, and Es. The proposed framework generalizes prior IRS–NOMA security analyses, which commonly presume ideal hardware or consider only a small number of Es. Moreover, Table 1 summarizes the relevant techniques applied in related works, and a comparison with the present paper highlights its distinct contribution.
- Joint reliability and security analysis: For a thorough assessment of system performance, we examine both the COP of legitimate users and the IP of Es, which allows us to clearly characterize the reliability–security trade-off in IRS-assisted NOMA systems.
- Closed-form analytical results over generalized fading channels: We obtain closed-form formulas for the COP and IP assuming Nakagami-m fading on the cascaded BS–IRS–user links and Rayleigh fading on the eavesdropper channels, explicitly accounting for distortion noise caused by hardware imperfections. These expressions extend earlier studies that either ignore HIs or adopt oversimplified channel models.
- Learning-assisted performance prediction: A feedforward DNN is constructed to estimate COP and IP using data generated via Monte Carlo simulations. Although related analytical–learning hybrid schemes exist in the literature, the proposed DNN is uniquely customized for the considered IRS–NOMA PLS framework and is demonstrated to accurately emulate the analytical results while offering lower computational complexity.
- Design insights through numerical analysis: We present numerical and simulation results to examine how key system parameters-such as the number of IRS elements, reflection coefficients, power allocation factors, signal-to-noise ratio (SNR), the number of Es, and HI parameters-affect performance, thereby providing practical guidance for the design of IRS-assisted NOMA systems.

The paper is structured into six sections. Section 2 describes the IRS-NOMA application and examines the system paradigm. In Section 3, we discuss system reliability based on COP. The security of the IP-based system is addressed in Section 4. Section 5 presents a DNN-based prediction of the main COP and IP. Representative numerical results are demonstrated in Section 6, and the paper concludes with Section 7.

To provide a rigorous basis for the proposed analysis, the following section establishes a comprehensive system model that accounts for IRS-NOMA transmission and the impact of HIs.

2. System Model

A secure cooperative IRS-NOMA system under the impact of HIs at all devices is considered, as illustrated in Figure 1. The system comprises a BS, an IRS with S reflecting elements, two users (D_i, $\{i = 1, 2\}$), and U Es [*] . We assume that the Es are located closer to

[*]This study adopts a passive E model, which is the most common assumption in PLS literature. The E only listens to

Tab. 1: Comparison of the paper with similar studies.

	Our work	[1]	[6]	[?]	[12]	[15]	[16]	[17]	[18]	[19]	[20]
IRS-OMA system	√			√	√			√		√	√
IRS-MOMA system	√	√	√	√	√	√	√	√	√	√	
HIs	√	√							√	√	
PLS	√	√	√	√	√	√	√	√	√	√	√
Multiple Es	√		√								
DNN	√			√							
COP	√			√		√				√	
IP	√			√		√					

"√" indicates references that cover this paper in detail.

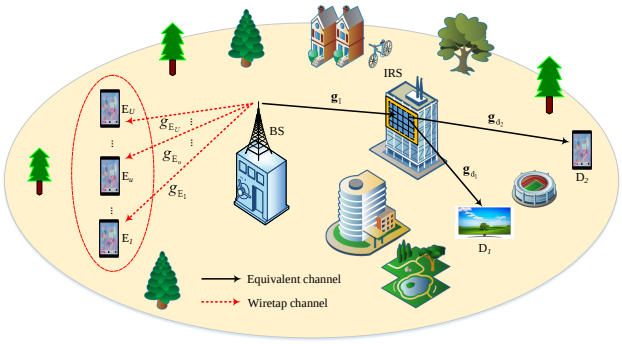

Fig. 1: The secure downlink system paradigm for a cooperative IRS-NOMA system.

the BS, allowing them to intercept signals from the BS but not from the IRS. The signal transmission process is as follows: the BS transmits signals to D_i through the IRS, while the Es simultaneously attempt to intercept the signals sent from the BS to D_i. Moreover, we assume that D_1 is positioned closer to both the IRS and the BS than D_2. In addition, there is no direct link from the BS to D_i due to obstacles such as buildings, large trees, or mountains [4]. Moreover, The IRS reflecting elements are divided into $S = S_1 + S_2$ [27], where S_1 elements are directed toward D_1 and S_2 elements toward D_2. Moreover, all channels experience quasi-static flat fading, and the channel state information (CSI) of each channel is assumed to be perfectly known at the BS [23, 28]. This assumption is commonly adopted in the literature and can be approached in practice when sufficiently long pilot sequences and adequate training overhead are provided. Moreover, the key parameters can be found in Table 2.

Tab. 2: Key parameters.

Symbol	Description
$\Pr(.)$	The probability operator
$F_X(.)$	The cumulative distribution function
$f_X(.)$	The probability distribution function
d_{BI}	The distances between the BS and the IRS
d_{BD_i}	The distances between the BS and D_i
d_{ID_i}	The distances between the IRS and D_i
d_{E_u}	The distances from the BS to the Es
λ	The path-loss exponents
ρ_i	The power allocation coefficients for D_i
v_i	The transmitted signals directed towards D_i
P_{B}	The transmit power of the BS
ϖ_{D_i}	The additive white Gaussian noises (AWGNs) at D_i with $\varpi_{\mathrm{D}_i} \sim CN(0, \psi_0)$
ϖ_{E_u}	The AWGNs present at Es with $\varpi_{\mathrm{E}_u} \sim CN(0, \psi_{\mathrm{E}})$
ψ_0, ψ_{E}	The noise variance
R_i	The target rates of D_i
g_{E_u}	The small-scale fading of the BS-to-Es link follows a Rayleigh fading model with $g_{\mathrm{E}_u} \sim CN\left(0, \mu_{g_{\mathrm{E}_u}}\right)$
g_i	The small-scale fading of the BS-to-D_1 link follows a Rayleigh fading model with $g_i \sim CN(0, \mu_{g_i})$

the BS-IRS-D_i link and does not transmit or interfere [?, 27]. Moreover, in this work, we assume that the E is equipped with a single antenna.

The signal received at the D_1 from the BS is described as [28]

$$q_{D_1} = \frac{\mathbf{g}_I \mathbf{\Phi}_1 \mathbf{g}_{d_1}}{\sqrt{d_{BI}^{\lambda} d_{ID_1}^{\lambda}}} \left(\sqrt{\rho_1 P_B} v_1 + \sqrt{\rho_2 P_B} v_2 + \varsigma_B \right) + \varsigma_{ID_1} + \varpi_{D_1}, \quad (1)$$

where the reflection coefficient matrix for the BS-IRS-D_i link[†] is denoted by $\mathbf{\Phi}_i = \text{diag}\left(\chi_1 e^{j\omega_1^{(D_i)}}, \ldots, \chi_{s_i} e^{j\omega_{s_i}^{(D_i)}}, \ldots, \chi_{S_i} e^{j\omega_{S_i}^{(D_i)}} \right)$, $\left(j = \sqrt{-1}\right)$, where $\chi_{S_i} \in [0,1]$ represents the amplitude-reflection coefficient and $\omega_{s_i}^{(D_i)} \in [0, 2\pi)$ denotes the adjustable phase shift variable of the s_i-th element, which the IRS can control with $s_i = (1, \ldots, S_i)$ [28]. Specifically, $\mathbf{g}_I = [g_{I,1}, g_{I,2}, \ldots, g_{I,w}]$, $(w \in \{S_1, S_2\})$, and $\mathbf{g}_{d_i} = \left[g_{d_{i,1}}, g_{d_{i,2}}, \ldots, g_{d_{i,S_i}}\right]^T$ represent the complex channel coefficients corresponding to BS-IRS, and IRS-D_i, respectively [28]. Each element within $\mathbf{g}_I$ and $\mathbf{g}_{d_i}$ follows the Nakagami-m fading model with distinct fading parameters, namely $m_{g_{I,s}}$ and $m_{g_{d_{i,s}}}$. It is important to note that a fixed power allocation sharing between the two user devices is assumed, with $\rho_1 < \rho_2$ to ensure user fairness, and $\rho_1 + \rho_2 = 1$ [30]. $\varsigma_B \sim CN\left(0, \wp_B^2 P_B\right)$ and $\varsigma_{ID_i} \sim CN\left(0, \wp_i^2 P_B |\mathbf{g}_I \mathbf{\Phi}_i \mathbf{g}_{d_i}|^2\right)$ represent distortion noise, where $\wp_B^2$ and $\wp_i^2$ denote the levels of residual HIs (RHIs) in the BS and D_i, respectively [31].

At D_1, the primary focus of the initial detection is on the signal v_2. The associated signal-to-interference-plus-noise ratio (SINR) is represented by

$$\gamma_{D_1}^{v_2} = \frac{|\mathbf{g}_I \mathbf{\Phi}_1 \mathbf{g}_{d_1}|^2 d_{BI}^{-\lambda} d_{ID_1}^{-\lambda} \rho_2 \kappa_B}{|\mathbf{g}_I \mathbf{\Phi}_1 \mathbf{g}_{d_1}|^2 \kappa_B \varepsilon_1 + 1}, \quad (2)$$

where $\kappa_B = \frac{P_B}{\psi_0}$, $\varepsilon_1 = d_{BI}^{-\lambda} d_{ID_1}^{-\lambda} \rho_1 + d_{BI}^{-\lambda} d_{ID_1}^{-\lambda} \wp_B^2 + \wp_1^2$.

After applying successive interference cancellation (SIC), the SINR for decoding the signal of D_1 is expressed as

$$\gamma_{D_1}^{v_1} = \frac{|\mathbf{g}_I \mathbf{\Phi}_1 \mathbf{g}_{d_1}|^2 d_{BI}^{-\lambda} d_{ID_1}^{-\lambda} \rho_1 \kappa_B}{|\mathbf{g}_I \mathbf{\Phi}_1 \mathbf{g}_{d_1}|^2 \varepsilon_2 \kappa_B + 1}, \quad (3)$$

where $\varepsilon_2 = d_{BI}^{-\lambda} d_{ID_1}^{-\lambda} \wp_B^2 + \wp_1^2$.

[†]In this study, we assume perfect CSI for all BS-IRS-D_i links and ideal, continuously adjustable IRS phase shifts [28,29]. This common assumption enables coherent phase alignment across IRS elements. It also facilitates a tractable analysis of the system's fundamental performance limits. Although practical systems can experience channel estimation errors, training overhead, and finite-bit IRS phase quantization, incorporating these impairments necessitates additional protocol-specific modeling, which is beyond the scope of this work. Instead, the presented results serve as a theoretical upper bound, while robustness analysis under imperfect CSI and quantized phase control is left for future research.

Similar to (1), the signal received at D_2 is expressed as [28]

$$q_{D_2} = \frac{\mathbf{g}_I \mathbf{\Phi}_2 \mathbf{g}_{d_2}}{\sqrt{d_{BI}^{\lambda} d_{ID_2}^{\lambda}}} \left(\sqrt{\rho_1 P_B} v_1 + \sqrt{\rho_2 P_B} v_2 + \varsigma_B \right) + \varsigma_{ID_2} + \varpi_{D_2}. \quad (4)$$

At this moment, the D_2 SINR for decoding its own signal is expressed as

$$\gamma_{D_2}^{v_2} = \frac{|\mathbf{g}_I \mathbf{\Phi}_2 \mathbf{g}_{d_2}|^2 d_{BI}^{-\lambda} d_{ID_2}^{-\lambda} \rho_2 \kappa_B}{|\mathbf{g}_I \mathbf{\Phi}_2 \mathbf{g}_{d_2}|^2 \varepsilon_3 \kappa_B + 1}, \quad (5)$$

where $\varepsilon_3 = d_{BI}^{-\lambda} d_{ID_2}^{-\lambda} \rho_1 + d_{BI}^{-\lambda} d_{ID_2}^{-\lambda} \wp_B^2 + \wp_2^2$.

The signal received at device Es is represented by the following expression [26]

$$q_{E_u} = \frac{g_{E_u}}{\sqrt{d_{E_u}^{\lambda}}} \left(\sqrt{\rho_1 P_B} v_1 + \sqrt{\rho_2 P_B} v_2 + \varsigma_B \right) + \varsigma_{BE_u} + \varpi_{E_u}, \quad (6)$$

where $\varsigma_{BE_u} \sim CN\left(0, \wp_{E_u}^2 P_B |g_{E_u}|^2\right)$ represents distortion noise, whereas $\wp_{E_u}^2$ denotes the levels of RHI in the Es [31].

Within the framework of Es, the SINR for decoding the signal of D_2 is defined as [26]

$$\gamma_{E_u}^{v_2} = \frac{\underbrace{\max_{1 \le u \le U}} \left(|g_{E_u}|^2 \right) d_{E_u}^{-\lambda} \rho_2 \kappa_E}{\underbrace{\max_{1 \le u \le U}} \left(|g_{E_u}|^2 \right) \varepsilon_4 \kappa_E + 1} = \frac{\tau_{BE} d_{E_u}^{-\lambda} \rho_2 \kappa_E}{\tau_{BE} \varepsilon_4 \kappa_E + 1}, \quad (7)$$

where $\kappa_E = \frac{P_B}{\psi_E}$, $\varepsilon_4 = d_{E_u}^{-\lambda} \rho_1 + d_{E_u}^{-\lambda} \wp_B^2 + \wp_{E_u}^2$, $\tau_{BE} = \underbrace{\max_{1 \le u \le U}} \left(|g_{E_u}|^2 \right)$ denotes the maximum gain of the channel from the BS to the Es [26].

After applying SIC, the SINR for decoding the signal of D_1 at Es is expressed as

$$\gamma_{E_u}^{v_1} = \frac{\tau_{BE} d_{E_u}^{-\lambda} \rho_1 \kappa_E}{\tau_{BE} \varepsilon_5 \kappa_E + 1}, \quad (8)$$

where $\varepsilon_5 = d_{E_u}^{-\lambda} \wp_B^2 + \wp_{E_u}^2$.

Building upon the established system model, we now proceed to derive exact closed-form expressions for the COP to evaluate the communication reliability of the legitimate users.

3. System Reliability Based on COP

In communication systems, the COP is defined as the likelihood that an outage will occur when a user's information rate falls below a predetermined target rate.

COP serves as a widely utilized metric for evaluating system performance in scenarios involving fixed-rate transmission. This section focuses on analyzing the outage performance of downlink IRS-NOMA networks.

3.1. COP of D_1

According to the NOMA principle, the COP of D_1 occurs when D_1 fails to successfully decode signals v_1 and v_2. In this context, the COP of D_1 is expressed as [32, 33]

$$\mathrm{COP}_{\mathrm{D}_1} = 1 - \Pr\left(\gamma_{\mathrm{D}_1}^{v_2} \geq \nu_2, \gamma_{\mathrm{D}_1}^{v_1} \geq \nu_1\right), \tag{9}$$

where $\nu_i = 2^{R_i} - 1$.

Theorem 1: The exact expression for the COP of D_1 is furnished by

$$\mathrm{COP}_{\mathrm{D}_1} = \exp\left(-\frac{\eta_{H_1}}{2}\right) \sum_{c=0}^{\infty} \frac{\eta_{H_1}^c \gamma\left(c+\frac{1}{2}, \frac{\Xi S_1(1-\sigma_1)}{2\chi^2}\right)}{c! 2^c \Gamma\left(c+\frac{1}{2}\right)}, \tag{10}$$

where $\eta_{H_1} = \frac{S_1\sigma_1}{1-\sigma_1}$, $\sigma_1 = \frac{1}{m_{g_{\mathrm{I},s}} m_{g_{\mathrm{d}_{1,s}}}} \left[\frac{\Gamma\left(m_{g_{\mathrm{I},s}}+1/2\right)}{\Gamma\left(m_{g_{\mathrm{I},s}}\right)}\right]^2 \left[\frac{\Gamma\left(m_{g_{\mathrm{d}_{1,s}}}+1/2\right)}{\Gamma\left(m_{g_{\mathrm{d}_{1,s}}}\right)}\right]^2$, $\Xi = \max\left[\frac{\nu_2}{\kappa_{\mathrm{B}}\left(d_{\mathrm{BI}}^{-\lambda} d_{\mathrm{ID}_1}^{-\lambda}\rho_2 - \nu_2\varepsilon_1\right)}, \frac{\nu_1}{\kappa_{\mathrm{B}}\left(d_{\mathrm{BI}}^{-\lambda} d_{\mathrm{ID}_1}^{-\lambda}\rho_1 - \nu_1\varepsilon_2\right)}\right]$.

Proof: Look at Appendix A.

3.2. COP of D_2

The occurrence of COP at D_2 arises when D_2 fails to successfully decode its own signal. At this point, the COP of D_2 is presented as [32, 34]

$$\mathrm{COP}_{\mathrm{D}_2} = 1 - \Pr\left(\gamma_{\mathrm{D}_2}^{v_2} \geq \nu_2\right). \tag{11}$$

Theorem 2: The exact expression for the COP of D_2 is furnished by

$$\mathrm{COP}_{\mathrm{D}_2} = \exp\left(-\frac{\eta_{H_2}}{2}\right) \times \sum_{c=0}^{\infty} \frac{\eta_{H_2}^c \gamma\left(c+\frac{1}{2}, \frac{\nu_2 S_2(1-\sigma_2)}{2\chi^2\kappa_{\mathrm{B}}\left(d_{\mathrm{BI}}^{-\lambda} d_{\mathrm{ID}_2}^{-\lambda}\rho_2 - \nu_2\varepsilon_3\right)}\right)}{c! 2^c \Gamma\left(c+\frac{1}{2}\right)}, \tag{12}$$

where $\eta_{H_2} = \frac{S_2\sigma_2}{1-\sigma_2}$, $\sigma_2 = \frac{1}{m_{g_{\mathrm{I},s}} m_{g_{\mathrm{d}_{2,s}}}} \left[\frac{\Gamma\left(m_{g_{\mathrm{I},s}}+1/2\right)}{\Gamma\left(m_{g_{\mathrm{I},s}}\right)}\right]^2 \left[\frac{\Gamma\left(m_{g_{\mathrm{d}_{2,s}}}+1/2\right)}{\Gamma\left(m_{g_{\mathrm{d}_{2,s}}}\right)}\right]^2$.

Proof: Look at Appendix B.

Remark 1: It can be clearly seen from (9)-(12) *that the COP performance depends on the power allocation factors and the number of IRS metasurface elements. Moreover, the threshold data rates also influence this performance. This analysis will be validated in the numerical simulation section.*

Beyond communication reliability, ensuring the confidentiality of information is crucial in the presence of Es. Therefore, the subsequent section focuses on evaluating the IP to characterize the system's security performance.

4. Security of the IP-based system

In addition to the system performance, as represented by the COP discussed in the preceding section, the security of the system can be assessed through an examination of the IP. Consequently, this section is dedicated to evaluating the security capability of the system by analyzing the IP associated with D_i.

4.1. IP study of D_1

According to (8), the IP for user D_1 is established when the SINR, represented by $\gamma_{\mathrm{E}_u}^{v_1}$, surpasses the specified threshold set for D_1. Consequently, the IP for D_1 can be articulated as

$$\mathrm{IP}_{\mathrm{D}_1} = \Pr\left(\gamma_{\mathrm{E}_u}^{v_1} \geq \nu_1\right). \tag{13}$$

Theorem 3: The exact expression of the IP at D_1 is furnished by

$$\mathrm{IP}_{\mathrm{D}_1} = \sum_{b=1}^{U} \binom{U}{b} (-1)^{b-1} \times \exp\left[-\frac{b\nu_1}{\kappa_{\mathrm{E}}\mu_{g_{\mathrm{E}_u}}\left(d_{\mathrm{E}_u}^{-\lambda}\rho_1 - \nu_1\varepsilon_5\right)}\right]. \tag{14}$$

Proof: Look at Appendix C.

4.2. IP study of D_2

In a manner analogous to (13), the IP of D_2 is articulated as

$$\mathrm{IP}_{\mathrm{D}_2} = \Pr\left(\gamma_{\mathrm{E}_u}^{v_2} \geq \nu_2\right). \tag{15}$$

Theorem 4: The exact expression of the IP at D_2 is furnished by

$$\mathrm{IP}_{\mathrm{D}_2} = \sum_{b=1}^{U} \binom{U}{b} (-1)^{b-1} \times \exp\left[-\frac{b\nu_2}{\kappa_{\mathrm{E}}\mu_{g_{\mathrm{E}_u}}\left(d_{\mathrm{E}_u}^{-\lambda}\rho_2 - \nu_2\varepsilon_4\right)}\right]. \tag{16}$$

Proof: Look at Appendix D.

Remark 2: It can be clearly seen from (13)-(16) *that the performance depends on several key factors. Specifically, increasing the SNR (κ_E) or reducing the communication distance degrades the users' security performance. Moreover, higher RHI levels at the Es improve the system's security. Increasing the number of Es also contributes to an overall enhancement in security performance.*

In the previous sections, we focused on the IRS-assisted links by assuming the direct links between the BS and the users are obstructed. To provide a more comprehensive evaluation, this section discusses an extended scenario where direct communication links are available, reflecting a more generalized wireless environment.

5. Extended IRS-NOMA system scenarios with a direct link

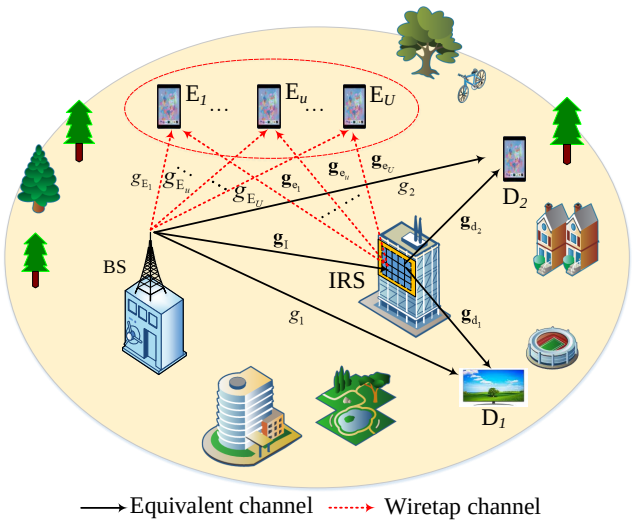

Fig. 2: The secure downlink system paradigm for a cooperative IRS-NOMA system with a direct link.

Building on the system depicted in Figure 1, we extend our analysis to the IRS-NOMA scenario with a direct link, as illustrated in Figure 2. Specifically, based on the configuration in Figure 1, we further consider the direct transmission path from the BS to user D_i. In addition, the Es are assumed to intercept not only the user's signals from the BS but also those reflected by the IRS. Consequently, D_i receives signals both directly from the BS and via the IRS, and the same applies to the Es.

The received signal at D_1 can be written as

$$\begin{aligned} q_{\mathrm{D}_1}^{(\mathrm{dl})} = & \left(\frac{\mathbf{g}_{\mathrm{I}} \mathbf{\Phi}_1 \mathbf{g}_{\mathrm{d}_1}}{\sqrt{d_{\mathrm{BI}}^{\lambda} d_{\mathrm{ID}_1}^{\lambda}}} + \frac{g_1}{\sqrt{d_{\mathrm{BD}_1}^{\lambda}}} \right) \\ & \times \left(\sqrt{\rho_1 P_{\mathrm{B}}} v_1 + \sqrt{\rho_2 P_{\mathrm{B}}} v_2 + \varsigma_{\mathrm{B}} \right) \\ & + \varsigma_{\mathrm{ID}_1} + \varsigma_{\mathrm{BD}_1} + \varpi_{\mathrm{D}_1}, \end{aligned} \tag{17}$$

where $\varsigma_{\mathrm{BD}_i} \sim CN\left(0, \wp_i^2 P_{\mathrm{B}} |g_i|^2\right)$ represent distortion noise.

Similar to (2), the signal of D_2 is detected first, and the corresponding SINR is expressed as (18), shown at the bottom of the next page.

After SIC, the signal of D_1 is decoded, and the corresponding SINR is given by (19), show at the bottom of the next page.

The received signal at D_2 can be given as

$$\begin{aligned} q_{\mathrm{D}_2}^{(\mathrm{dl})} = & \left(\frac{\mathbf{g}_{\mathrm{I}} \mathbf{\Phi}_2 \mathbf{g}_{\mathrm{d}_2}}{\sqrt{d_{\mathrm{BI}}^{\lambda} d_{\mathrm{ID}_2}^{\lambda}}} + \frac{g_2}{\sqrt{d_{\mathrm{BD}_2}^{\lambda}}} \right) \\ & \times \left(\sqrt{\rho_1 P_{\mathrm{B}}} v_1 + \sqrt{\rho_2 P_{\mathrm{B}}} v_2 + \varsigma_{\mathrm{B}} \right) \\ & + \varsigma_{\mathrm{ID}_2} + \varsigma_{\mathrm{BD}_2} + \varpi_{\mathrm{D}_2}. \end{aligned} \tag{20}$$

At D_2, its signal is decoded directly by regarding D_1's signal as interference, and its SINR is written as (21), shown at the bottom of the next page.

The signal received at Es is represented as

$$\begin{aligned} q_{\mathrm{E}_u}^{(\mathrm{dl})} = & \left(\frac{\mathbf{g}_{\mathrm{I}} \mathbf{\Phi}_{\mathrm{e},u} \mathbf{g}_{\mathrm{e}_u}}{\sqrt{d_{\mathrm{BI}}^{\lambda} d_{\mathrm{IE}_u}^{\lambda}}} + \frac{g_{\mathrm{E}_u}}{\sqrt{d_{\mathrm{E}_u}^{\lambda}}} \right) \\ & \times \left(\sqrt{\rho_1 P_{\mathrm{B}}} v_1 + \sqrt{\rho_2 P_{\mathrm{B}}} v_2 + \varsigma_{\mathrm{B}} \right) \\ & + \varsigma_{\mathrm{IE}_u} + \varsigma_{\mathrm{BE}_u} + \varpi_{\mathrm{E}_u}. \end{aligned} \tag{22}$$

where $\varsigma_{\mathrm{IE}_u} \sim CN\left(0, \wp_{\mathrm{E}_u}^2 P_{\mathrm{B}} |\mathbf{g}_{\mathrm{I}} \mathbf{\Phi}_{\mathrm{e},u} \mathbf{g}_{\mathrm{e}_u}|^2\right)$ denotes distortion noise. The reflection coefficient matrix for the BS-IRS-Es link is denoted by $\mathbf{\Phi}_{\mathrm{e},u} = \mathrm{diag}\left(\chi_1 e^{j\omega_1^{(\mathrm{E}_1)}}, \chi_2 e^{j\omega_2^{(\mathrm{E}_2)}}, \ldots, \chi_d e^{j\omega_d^{(\mathrm{E}_u)}}\right)$. To identify D_2's communication, the E's received SINR can be given by (23), shown at the bottom of the next page.

After SIC, the SINR that the Es acquired to identify D_1's signal is given as (24), shown at the bottom of the next page.

Next, we assume that $\left| d_{\mathrm{BI}}^{-\frac{\lambda}{2}} d_{\mathrm{ID}_i}^{-\frac{\lambda}{2}} \mathbf{g}_{\mathrm{I}} \mathbf{\Phi}_i \mathbf{g}_{\mathrm{d}_i} + d_{\mathrm{BD}_i}^{-\frac{\lambda}{2}} g_i \right|^2 \approx \left(d_{\mathrm{BI}}^{-\lambda} d_{\mathrm{ID}_i}^{-\lambda} |\mathbf{g}_{\mathrm{I}} \mathbf{\Phi}_i \mathbf{g}_{\mathrm{d}_i}|^2 + d_{\mathrm{BD}_i}^{-\lambda} |g_i|^2 \right)$ and $\left| d_{\mathrm{BI}}^{-\frac{\lambda}{2}} d_{\mathrm{IE}_u}^{-\frac{\lambda}{2}} \mathbf{g}_{\mathrm{I}} \mathbf{\Phi}_{\mathrm{e},u} \mathbf{g}_{\mathrm{e}_u} + d_{\mathrm{E}_u}^{-\frac{\lambda}{2}} g_{\mathrm{E}_u} \right|^2 \approx$

$$\gamma_{\mathrm{D}_1}^{(\mathrm{dl},v_2)} = \frac{\left| d_{\mathrm{BI}}^{-\frac{\lambda}{2}} d_{\mathrm{ID}_1}^{-\frac{\lambda}{2}} \mathbf{g}_{\mathrm{I}} \mathbf{\Phi}_1 \mathbf{g}_{\mathrm{d}_1} + d_{\mathrm{BD}_1}^{-\frac{\lambda}{2}} g_1 \right|^2 \rho_2 \kappa_{\mathrm{B}}}{\left| d_{\mathrm{BI}}^{-\frac{\lambda}{2}} d_{\mathrm{ID}_1}^{-\frac{\lambda}{2}} \mathbf{g}_{\mathrm{I}} \mathbf{\Phi}_1 \mathbf{g}_{\mathrm{d}_1} + d_{\mathrm{BD}_1}^{-\frac{\lambda}{2}} g_1 \right|^2 (\rho_1 + \wp_{\mathrm{B}}^2) \kappa_{\mathrm{B}} + \wp_1^2 \kappa_{\mathrm{B}} |\mathbf{g}_{\mathrm{I}} \mathbf{\Phi}_1 \mathbf{g}_{\mathrm{d}_1}|^2 + \wp_1^2 \kappa_{\mathrm{B}} |g_1|^2 + 1}. \tag{18}$$

$$\gamma_{\mathrm{D}_1}^{(\mathrm{dl},v_1)} = \frac{\left| d_{\mathrm{BI}}^{-\frac{\lambda}{2}} d_{\mathrm{ID}_1}^{-\frac{\lambda}{2}} \mathbf{g}_{\mathrm{I}} \mathbf{\Phi}_1 \mathbf{g}_{\mathrm{d}_1} + d_{\mathrm{BD}_1}^{-\frac{\lambda}{2}} g_1 \right|^2 \rho_1 \kappa_{\mathrm{B}}}{\left| d_{\mathrm{BI}}^{-\frac{\lambda}{2}} d_{\mathrm{ID}_1}^{-\frac{\lambda}{2}} \mathbf{g}_{I} \mathbf{\Phi}_1 \mathbf{g}_{\mathrm{d}_1} + d_{\mathrm{BD}_1}^{-\frac{\lambda}{2}} g_1 \right|^2 \kappa_{\mathrm{B}} \wp_{\mathrm{B}}^2 + \wp_1^2 \kappa_{\mathrm{B}} |\mathbf{g}_{\mathrm{I}} \mathbf{\Phi}_1 \mathbf{g}_{\mathrm{d}_1}|^2 + \wp_1^2 \kappa_{\mathrm{B}} |g_1|^2 + 1}. \tag{19}$$

$\left(d_{\mathrm{BI}}^{-\lambda} d_{\mathrm{IE}_u}^{-\lambda} |\mathbf{g}_{\mathrm{I}} \mathbf{\Phi}_{\mathrm{e},u} \mathbf{g}_{\mathrm{e}_u}|^2 + d_{\mathrm{E}_u}^{-\lambda} |g_{\mathrm{E}_u}|^2 \right)$ [35]. Moreover, the phase parameters of the BS-IRS-Es link is optimized similar to (31), we have

$$|\mathbf{g}_{\mathrm{I}} \mathbf{\Phi}_{\mathrm{e},u} \mathbf{g}_{\mathrm{e}_u}|^2 = \chi^2 \left(\sum_{s=1}^{w} \left| \mathbf{g}_{\mathrm{I},s} \mathbf{g}_{\mathrm{e}_{u,s}} \right| \right)^2, \tag{25}$$

where we assume the conditions $\chi_s = \chi$ and $\forall_s$ without any loss of generality [28]. Moreover, similar to the case without a direct link, we assume that the channels from BS-E_u and from BS-IRS-E_u are maximized and selected as the best available links [26].

Similar to (9), the COP of D_1 occurs when D_1 fails to decode signals v_2 and v_1 successfully. Therefore, the COP of D_1 can be written as

$$\mathrm{COP}_{\mathrm{D}_1}^{(\mathrm{dl})} = 1 - \Pr\left(\gamma_{\mathrm{D}_1}^{(\mathrm{dl},v_2)} \geq \nu_2, \gamma_{\mathrm{D}_1}^{(\mathrm{dl},v_1)} \geq \nu_1 \right). \tag{26}$$

Next, similar to (11), the occurrence of COP at D_2 arises when D_2 fails to decode its own signal successfully. Therefore, the COP at D_2 can be given as

$$\mathrm{COP}_{\mathrm{D}_2}^{(\mathrm{dl})} = 1 - \Pr\left(\gamma_{\mathrm{D}_2}^{(\mathrm{dl},v_2)} \geq \nu_2 \right). \tag{27}$$

Similar to (13), the IP of D_i in the direct-link case can be articulated as

$$\mathrm{IP}_{\mathrm{D}_i}^{(\mathrm{dl})} = \Pr\left(\gamma_{\mathrm{E}_u}^{(\mathrm{dl},v_i)} \geq \nu_i \right). \tag{28}$$

The operational principles of the proposed IRS-NOMA systems with direct-link NOMA have been presented above. As shown, the proposed systems can be extended beyond this baseline configuration. Due to space limitations, the performance analysis of the extended system is not included in this section. Future work will further develop and provide a comprehensive analysis of the extended system. These extended configurations also highlight the adaptability of the IRS-NOMA framework under diverse deployment conditions.

Although the analytical formulas derived in previous sections provide precise results, their computational complexity can be high for real-time applications. To address this, the following section introduces a DNN architecture designed to offer fast and accurate performance predictions.

6. DNN-based prediction of main COP and IP

In this section, a DNN model is constructed to assess the COP and IP. The DNN serves as a data-driven alternative for complex system models where conventional mathematical derivations prove difficult to execute. While we have derived precise expressions for COP and IP within this paper, our objective is to further investigate the application of DNNs in this system model. This methodology aims to improve the precision of predictions while simultaneously minimizing the duration of execution [**?**].

The proposed hybrid approach integrates traditional analytical modeling with a DNN, thereby creating a comprehensive framework for performance prediction. The implementation of data-driven learning methodologies substantially augments the accuracy and robustness of the DNN within the analytical model, particularly in intricate scenarios. Moreover, the adaptability of the proposed DNN framework is examined, illustrating its potential for extension to other complex systems with appropriate modifications.

The principal contributions of this study are twofold: firstly, the derivation of analytical expressions for essential performance metrics, and secondly, the introduction of a complementary DNN model that augments these findings. This integration effectively harnesses the advantages of both traditional and contemporary methodologies, providing a robust solution for performance evaluation in intricate communication systems.

6.1. Description of the DNN architecture

The DNN model utilized in this context is a feed-forward neural network. For a detailed examination of

$$\gamma_{\mathrm{D}_2}^{(\mathrm{dl},v_2)} = \frac{\left| d_{\mathrm{BI}}^{-\frac{\lambda}{2}} d_{\mathrm{ID}_2}^{-\frac{\lambda}{2}} \mathbf{g}_{\mathrm{I}} \mathbf{\Phi}_2 \mathbf{g}_{\mathrm{d}_2} + d_{\mathrm{BD}_2}^{-\frac{\lambda}{2}} g_2 \right|^2 \rho_2 \kappa_{\mathrm{B}}}{\left| d_{\mathrm{BI}}^{-\frac{\lambda}{2}} d_{\mathrm{ID}_1}^{-\frac{\lambda}{2}} \mathbf{g}_{\mathrm{I}} \mathbf{\Phi}_2 \mathbf{g}_{\mathrm{d}_2} + d_{\mathrm{BD}_2}^{-\frac{\lambda}{2}} g_2 \right|^2 \kappa_{\mathrm{B}} \left(\rho_1 + \wp_{\mathrm{B}}^2\right) + \wp_2^2 \kappa_{\mathrm{B}} |\mathbf{g}_{\mathrm{I}} \mathbf{\Phi}_2 \mathbf{g}_{\mathrm{d}_2}|^2 + \wp_2^2 \kappa_{\mathrm{B}} |g_2|^2 + 1}. \tag{21}$$

$$\gamma_{\mathrm{E}_u}^{(\mathrm{dl},v_2)} = \frac{\left| d_{\mathrm{BI}}^{-\frac{\lambda}{2}} d_{\mathrm{IE}_u}^{-\frac{\lambda}{2}} \mathbf{g}_{\mathrm{I}} \mathbf{\Phi}_{\mathrm{e},u} \mathbf{g}_{\mathrm{e}_u} + d_{\mathrm{E}_u}^{-\frac{\lambda}{2}} g_{\mathrm{E}_u} \right|^2 \rho_2 \kappa_{\mathrm{E}}}{\left| d_{\mathrm{BI}}^{-\frac{\lambda}{2}} d_{\mathrm{IE}_u}^{-\frac{\lambda}{2}} \mathbf{g}_{\mathrm{I}} \mathbf{\Phi}_{\mathrm{e},u} \mathbf{g}_{\mathrm{e}_u} + d_{\mathrm{E}_u}^{-\frac{\lambda}{2}} g_{\mathrm{E}_u} \right|^2 \left(\rho_1 + \wp_{\mathrm{B}}^2\right) \kappa_{\mathrm{E}} + \wp_{\mathrm{E}_u}^2 \kappa_{\mathrm{E}} |g_{\mathrm{E}_u}|^2 + \wp_{\mathrm{E}_u}^2 \kappa_{\mathrm{E}} |\mathbf{g}_{\mathrm{I}} \mathbf{\Phi}_{\mathrm{e},u} \mathbf{g}_{\mathrm{e}_u}|^2 + 1}. \tag{23}$$

the DNN's configuration, please consult Figure 3. The architecture of the DNN comprises several layers, including an input layer, multiple hidden layers denoted as H_{dn}, and an output layer. The roles of each layer in the process of training the DNN model with sample datasets are succinctly outlined in references [36].

- The primary function of the input layer is to receive the input data, allowing the DNN model to establish the mapping between system parameters and their corresponding COP/IP values (the remaining DNN training cases follow the same process). Neurons in the input layer do not employ any activation function, and their number matches the number of system parameters.
- The hidden layers focus on computing the relationship between the input data and output data. Each connection within these hidden neurons possesses distinct weights and biases, enabling the network model to form nonlinear relationships. A nonlinear activation function is integrated into each hidden layer to enhance the expressive power of the model.
- The responsibility of the output layer is to predict the COP/IP by aggregating the information processed through the multiple hidden layers. Consequently, the output layer consist single neuron. Similar to the input layer, the neuron in the output layer does not employ any activation function.

In this model, the primary system parameters are transmitted to the server to be used as input values, each corresponding to one of the 22 neurons detailed in Table 3. The output layer, which comprises a single neuron, is employed to generate predictions for COP/IP. This process involves applying a linear function alongside its associated activation function, as referenced in [36,38]. Furthermore, 22 neurons align with the 22 input features (parameters being solely weight and bias). In the hidden layers referred to as layer r with $r = 1, \ldots, \mathrm{H}_{\mathrm{dn}}$, there are dn neurons, and the system employs the rectified linear unit (ReLU) function as its activation function.

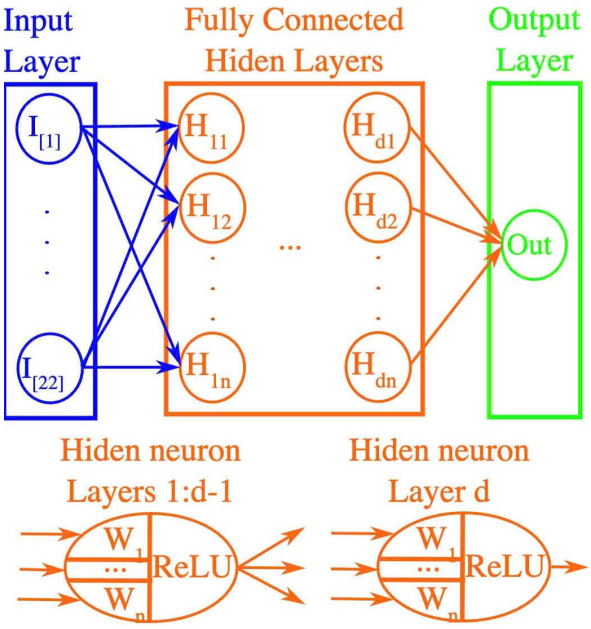

Fig. 3: The operational architecture of the DNN for the system [36, 39].

Remark 3 (Sensitivity Analysis): Although the DNN model incorporates 22 input features as detailed in Table 3, a sensitivity analysis was performed to evaluate their individual contributions. The results reveal that the transmit SNR (κ_{B}, κ_{E}) and the number of IRS elements (S) exhibit the highest feature importance scores. This confirms that the model accurately captures the physical essence of the IRS-NOMA system, where these two parameters primarily dictate the SINR and beamforming gains, respectively.

6.2. Data Set Construction

The Mean Square Error (MSE) was employed to assess the performance of the DNN. The MSE is calculated as [36,38]

$$\mathrm{MSE} = \frac{1}{|\nabla_{\mathrm{tes}}|} \sum_{r=0}^{|\nabla_{\mathrm{tes}}|-1} (\mathrm{Out} - \mathrm{Out}_{\mathrm{s}}). \tag{29}$$

$$\gamma_{\mathrm{E}_u}^{(\mathrm{dl},v_1)} = \frac{\left|d_{\mathrm{BI}}^{-\frac{\lambda}{2}} d_{\mathrm{IE}_u}^{-\frac{\lambda}{2}} \mathbf{g}_{\mathrm{I}} \mathbf{\Phi}_{\mathrm{e},u} \mathbf{g}_{\mathrm{e}_u} + d_{\mathrm{E}_u}^{-\frac{\lambda}{2}} g_{\mathrm{E}_u}\right|^2 \rho_1 \kappa_{\mathrm{E}}}{\left|d_{\mathrm{BI}}^{-\frac{\lambda}{2}} d_{\mathrm{IE}_u}^{-\frac{\lambda}{2}} \mathbf{g}_{\mathrm{I}} \mathbf{\Phi}_{\mathrm{e},u} \mathbf{g}_{\mathrm{e}_u} + d_{\mathrm{E}_u}^{-\frac{\lambda}{2}} g_{\mathrm{E}_u}\right|^2 \wp_{\mathrm{B}}^2 \kappa_{\mathrm{E}} + \wp_{\mathrm{E}_u}^2 \kappa_{\mathrm{E}} |g_{\mathrm{E}_u}|^2 + \wp_{\mathrm{E}_u}^2 \kappa_{\mathrm{E}} |\mathbf{g}_{\mathrm{I}} \mathbf{\Phi}_{\mathrm{e},u} \mathbf{g}_{\mathrm{e}_u}|^2 + 1}. \tag{24}$$

Tab. 3: System parameters used by the DNN for both training and testing [?, 23, 28, 36].

Inputs	Values	Inputs	Values
$\kappa_{\mathrm{B}} = \kappa_{\mathrm{E}}$	[20:40] dB	$m_{g_{\mathrm{d}_{1,s}}}$	2
ρ_1	0.3	$m_{g_{\mathrm{d}_{2,s}}}$	2
ρ_2	0.7	$\wp_{\mathrm{B}}$	0.01
R_1	0.1 bps/Hz	$\wp_1$	0.01
R_2	0.1 bps/Hz	$\wp_2$	0.01
λ	2	$\wp_{\mathrm{E}_u}$	0.01
d_{BI}	5 m	χ	0.9
d_{ID_1}	10 m	S_1	30
d_{ID_2}	20 m	S_2	30
d_{E_u}	20 m	U	3
$m_{g_{\mathrm{I},s}}$	2		

where, to assess the performance of the proposed DNN approach, we employ Algorithm 1 as detailed in Appendix E. This algorithm serves as a framework for executing the essential steps required for both training and evaluating the DNN. Moreover, the server associated with the BS processes r samples from our dataset, with the relationship between input and output denoted as $\mathrm{Da}_{[r]} = [\mathrm{I}_{[r]}, \mathrm{Out}_{\mathrm{s}}]$. Here, $\mathrm{I}_{[r]}$ represents a feature vector encompassing all input parameters detailed in Table 3. Monte-Carlo simulations employ this feature vector $\mathrm{I}_{[r]}$ to produce an anticipated secure metric referred to as $\mathrm{Out}_{\mathrm{s}}$. In conclusion, we compile a total of 5×10^5 data points and integrate them to construct the dataset. This dataset is then divided into three distinct subsets [23,36]: 80% allocated for training (∇_{tra}), 10% for validation (∇_{va}), and 10% for testing (∇_{tes}).

In the following section, we provide extensive numerical results and simulations to validate the accuracy of our theoretical derivations and to assess the effectiveness of the proposed DNN framework under various system configurations.

7. Results and Discussion

This section presents numerical findings that illustrate the performance assessment of the network under consideration. Additionally, the accuracy is periodically verified through Monte Carlo simulations. The terms "Sim." and "Ana." are abbreviations for simulation and analytical, respectively. Unless explicitly stated otherwise, the main parameters for the Monte Carlo simulations have been established as follows [?, 23, 28, 36, 37]: $\rho_1 = 0.3$, $R_i = 0.1$ bps/Hz, $\lambda = 2$, $d_{\mathrm{BI}} = 5$ m, $d_{\mathrm{ID}_1} = 10$ m, $d_{\mathrm{ID}_2} = 20$ m, $d_{\mathrm{E}_u} = 20$ m, $m_{g_{\mathrm{I},s}} = m_{g_{\mathrm{d}_{i,s}}} = 2$, $\wp_{\mathrm{B}} = \wp_i = \wp_{\mathrm{E}_u} = 0.01$, $\chi = 0.9$, $S_1 = S_2 = 30$, $U = 3$.

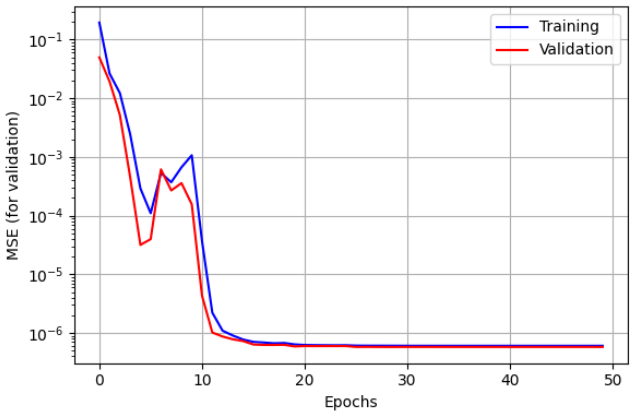

Fig. 4: The convergence of MSE for COP of D_1 during the training and validation of DNN.

By comparing the training and validation sets' curves, Figure 4 confirms that the DNN achieves the expected accuracy. Moreover, there is a near alignment between these two curves. This alignment shows that the MSE can get close to its lowest error level, which is reached when 20 epochs have passed. Moreover, the remaining cases, such as the COP of D_2 and the IP of D_i, verify that the DNN achieves the expected accuracy in the same manner as the COP of D_1.

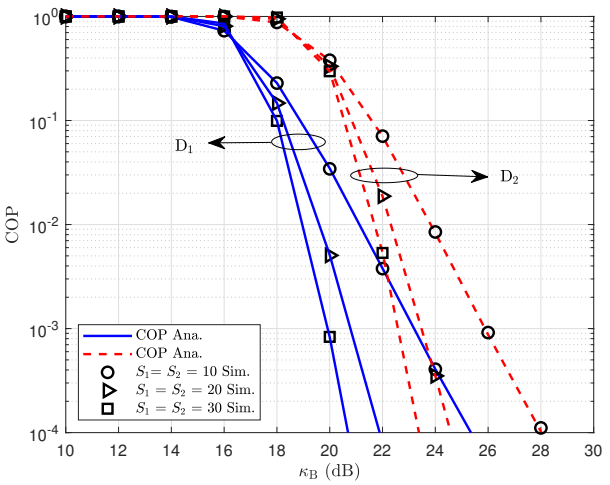

Fig. 5: COP of D_1 and D_2 versus κ_{B} for different $S_1 = S_2$.

Figure 5 presents the COP of user D_i as a function of parameter κ_{B}, evaluated under various values of $S_1 =$

S_2. The simulation results demonstrate an exceptional concordance with the analytical expressions and theoretical analysis. This alignment has been rigorously verified through Monte Carlo simulations, which are based on equations (9)-(12). The data presented in the figure indicate that the COP for D_1 markedly decreases as the κ_B increases from 26 dB to 37 dB. Similarly, D_2's COP follows a decreasing trend with an increase in κ_B from 30 dB to 41 dB. This phenomenon can be attributed to the fact that a higher transmit SNR enhances signal quality, thereby improving reception performance for D_i. Consequently, the likelihood of D_i's instantaneous SINR falling below the target threshold diminishes. Although D_1, being closer, generally benefits more due to favorable channel conditions, D_i experiences a significant reduction in COP as transmit SNR increases because noise and fading effects become less pronounced in high-SNR environments. Moreover, it is important to observe that as the number of reflecting elements in the IRS increases, there is a notable reduction in the COP for D_i within the system's operational parameters. This enhancement arises because a greater quantity of IRS elements amplifies the overall reflection gain, thereby enabling more effective manipulation of the wireless propagation environment. Specifically, with an increased number of reflecting elements, the IRS can execute more precise phase adjustments, which strengthen constructive signal combination at the receiver and mitigate fading and interference effects. As a result, there is an improvement in the received SNR, reducing the likelihood that the instantaneous SNR will fall below the required threshold. Thus, augmenting the number of IRS elements significantly decreases outage probability for D_i, highlighting one of the principal benefits of deploying a large-scale IRS.

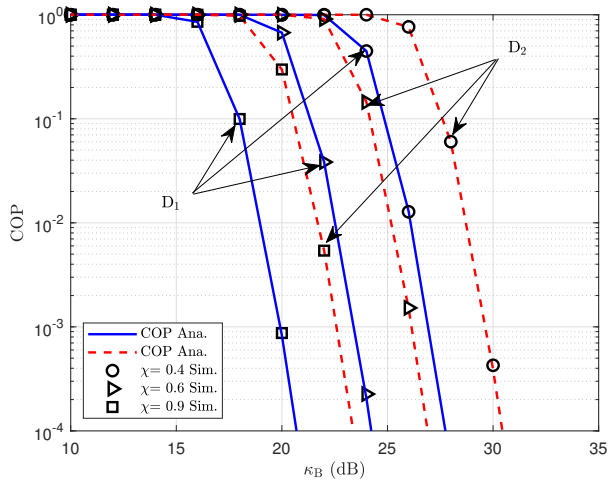

Fig. 6: COP of D_1 and D_2 versus κ_B for different χ.

Figure 6 presents the COP for D_i as a function of parameter κ_B across varying values of χ. Consistent with the findings depicted in Figure 5, it is evident that the COP for D_i experiences a substantial decline as κ_B increases. Furthermore, it is noteworthy that the COP for D_1 remains significantly lower than that of D_2 when κ_B ranges from 26 dB to 44 dB. A critical observation from this figure is that within the system's operating region, an increase in χ also results in a marked decrease in the COP for D_i. This trend can be attributed to the fact that a higher amplitude-reflection coefficient of the IRS allows for greater power reflection from incident signals, thereby enhancing the strength of reflected links toward intended users. In essence, a larger reflection coefficient augments the effective channel gain between the BS and D_i by fortifying the constructive combination of direct and reflected signal components. Consequently, this results in an improved received SNR, diminishing the probability that the instantaneous SNR will fall below the required threshold. Therefore, increasing the amplitude-reflection coefficient leads to superior signal quality, enhanced link reliability, and a notable reduction in system COP.

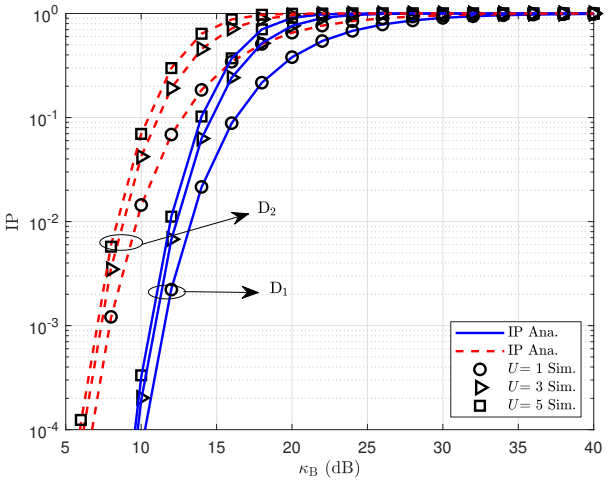

Fig. 7: IP of D_1 and D_2 versus κ_E for different U.

Figure 7 illustrates the IP of D_i as a function of parameter κ_E under different values of U. From the figure, it can be observed that as κ_E increases from 20 dB to approximately 34 dB, the IP of D_i increases significantly and then gradually reaches a saturation level beyond this point. This behavior can be explained by the fact that a higher SNR enhances the received signal strength not only at the legitimate D_i but also at potential Es. In the low-SNR region, even small increases in SNR considerably improve the received power, leading to a higher likelihood that the E's channel capacity exceeds the target secrecy rate, thereby increasing the IP. However, as the SNR continues to rise, both the legitimate and eavesdropping channels improve proportionally, resulting in a limited additional gain in IP. Consequently, the IP tends to stabilize and reach a saturation point in the high-SNR region, reflecting the in-

herent trade-off between reliability and security in the system. Furthermore, it is worth noting that as U increases, the IP of D_i also rises significantly. This occurs because a larger number of Es increases the likelihood that at least one of them will experience a favorable channel condition, enabling successful interception of the confidential information. In other words, with more eavesdropping devices present in the environment, the probability that one eavesdropper achieves a higher received SNR than the legitimate user becomes higher. As a result, the overall system security degrades, leading to a noticeable increase in IP as the number of Es grows.

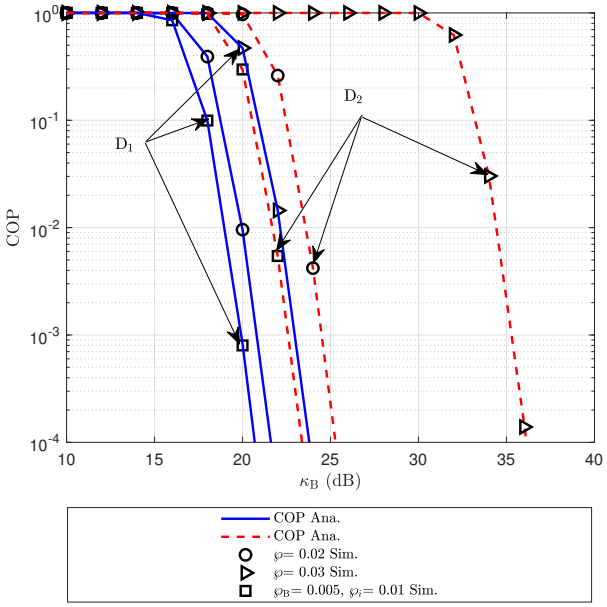

(a) COP for D_i

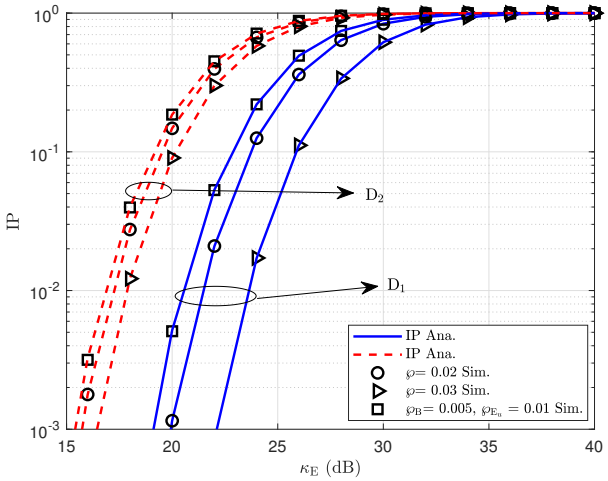

(b) IP for D_i

Fig. 8: The trade-off between the COP and IP of D_1 and D_2 is analyzed with respect to SNR for different $\wp$=$\wp_{\mathrm{B}}$ = $\wp_i$ = $\wp_{\mathrm{E}_u}$.

Figure 8 illustrates the trade-off between the COP and IP of D_i with respect to the SNR and different values of $\wp$=$\wp_{\mathrm{B}}$ = $\wp_i$ = $\wp_{\mathrm{E}_u}$. Similar to the previous figures, it can be observed that as the SNR increases from 26 dB to 39 dB, the COP of D_i significantly decreases. However, this comes at the expense of the IP, which notably increases as the SNR rises from 20 dB to 38 dB. This indicates that higher SNR values enhance the ability to receive signals but simultaneously increase the likelihood of eavesdropping. An important observation from this figure is that when the value of $\wp$ increases from 0.02 to 0.03, the COP of D_i also increases, while the IP of D_i decreases. This can be explained by the fact that when the hardware impairment level increases, the overall signal quality deteriorates due to additional distortion and noise introduced by imperfect transceiver components. Consequently, the effective SINR at legitimate D_i decreases, leading to a higher COP. Conversely, the E's received signal is also affected by the same impairment, resulting in a lower SINR and, therefore, a reduced IP. Hence, increasing hardware impairment degrades system reliability while enhancing PLS. Moreover, when considering asymmetric HIs (i.e., $\wp_{\mathrm{B}}$ = 0.005, $\wp_i$ = 0.01, $\wp_{\mathrm{E}_u}$ = 0.01), it can be observed that the COP of D_1 is approximately lower than 30% that obtained under the symmetric case where all distortion noise coefficients are set equal ($\wp$ = 0.01) at SNR = 20 dB, while the corresponding IP of D_1 increases by about 8% relative to its symmetric counterpart. In addition, because the analytical expressions are kept in symbolic closed form, all HI values can be trivially substituted; however, this work focuses on other key parameters, so HI values are fixed for clarity.

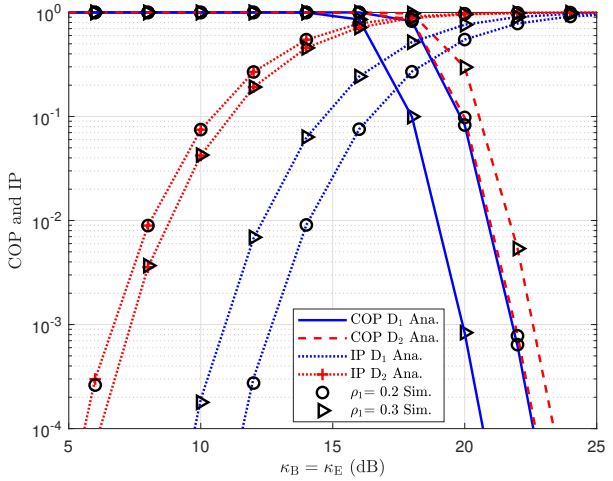

Fig. 9: The trade-off between the COP and IP of D_1 and D_2 is analyzed with respect to κ_{B}= κ_{E} for different ρ_1.

Figure 9 illustrates the trade-off between the COP and IP of D_i with respect to the variation of κ_{B}= κ_{E} and for different values of ρ_1. Similar to the observa-

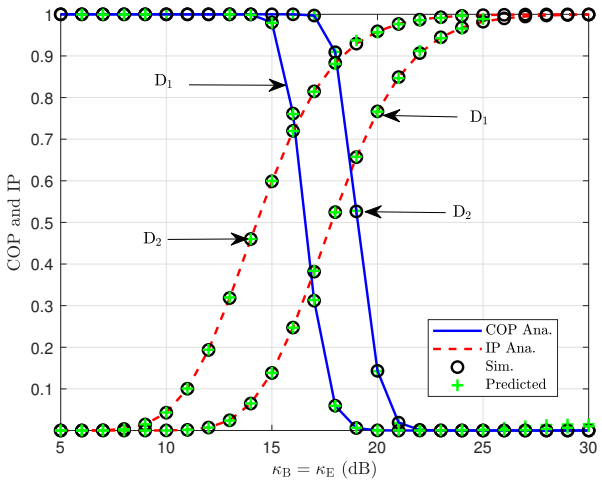

Fig. 10: Trade-off between the COP and IP of D_1 and D_2 in conjunction with DNN with respect to $\kappa_B = \kappa_E$.

tions from the previous figures, it can be seen that as $\kappa_B = \kappa_E$ increases, the COP of D_i decreases significantly, whereas the IP of D_i increases noticeably, showing a clear trade-off between reliability and security. Moreover, D_1 exhibits a considerably lower COP compared to D_2 within the system's operating region. Likewise, the IP of D_1 is also much lower than that of D_2 as $\kappa_B = \kappa_E$ increases from 20 dB to around 36 dB, after which it reaches a saturation point. Another important observation in this figure is that when ρ_1 increases from 0.2 to 0.3, the COP of D_1 decreases significantly, while the COP of D_2 increases. In contrast, for the IP, as ρ_1 rises from 0.2 to 0.3, the IP of D_1 increases noticeably, whereas that of D_2 decreases significantly.

Using the DNN-based prediction, Figure 10 shows the trade-off between the COP and IP as a function of SNR. As in Figure 9, as the SNR rises from 26 dB to 36 dB, the COP dramatically drops, whereas the IP shows a notable improvement when the SNR increases from 22 dB to 38 dB. One notable observation from this figure is the discrepancy between the actual outcomes and those predicted by the DNN. The COP and IP curves closely align with the DNN prediction patterns, indicating a substantial level of concordance between the analytical results and those anticipated by the model.

Table 4 presents a quantitative assessment of the DNN model's performance on the unseen test set. It can be observed that the RMSE and MAE for both COP and IP predictions are remarkably low (below 0.003), indicating a minimal deviation from the analytical benchmarks. Furthermore, the Coefficient of Determination (R^2) values for both metrics exceed 0.999, which signifies that the DNN model can explain over 99.9% of the variance in the system's performance.

Tab. 4: Quantitative Performance Metrics of the DNN Model.

Metric	Description	COP Prediction	IP Prediction
RMSE	Root Mean Square Error	2.1×10^{-3}	1.9×10^{-3}
MAE	Mean Absolute Error	1.5×10^{-3}	1.4×10^{-3}
R^2	Coefficient of Determination	0.9992	0.9995

These numerical results, alongside the visual parity shown in Figure 10, confirm that the trained DNN is a highly reliable surrogate model, capable of replacing complex analytical derivations for real-time performance estimation in IRS-NOMA networks.

Figure 11 illustrates the COP of D_i with respect to the SNR factor for four baseline schemes: IRS-NOMA with HIs (Scheme 1), OMA with IRS (Scheme 2), NOMA without IRS (Scheme 3), and IRS-NOMA without HIs (Scheme 4). From the figure, it can first be observed that as the SNR increases, the COP of all four schemes decreases within the system's operating range, and the COP of D_1 is consistently lower than that of D_2. When comparing scheme 1 and scheme 2, the COP of D_1 under scheme 1 is lower than that under scheme 2, whereas the opposite trend is observed for D_2. When comparing scheme 1 with scheme 3, the COP of D_i under scheme 1 is higher than that of scheme 3 when the SNR increases from 10 dB to approximately 20 dB. However, when the SNR increases from about 20 dB to 30 dB, the COP of scheme 1 becomes lower than that of scheme 3. Finally, when comparing Scheme 1 and Scheme 4, it can be seen that the COP of D_i under Scheme 1 is higher than that of Scheme 4 when the SNR increases from approximately 14 dB to 24 dB.

The trade-off between the COP and IP of D_1 and D_2 versus SNR for the direct-link and no-direct-link scheme is illustrated in Figure 12. As observed in the Figure, the COP of D_1 is lower than that of D_2 within the system's operating region. It is shown that when SNR increases from 3 dB to 16 dB for user D_1, the COP achieved with the direct-link scheme remains lower than that of the no-direct-link scheme. Furthermore, the COP of D_i for both schemes becomes lower than that of the direct-link scheme when SNR increases from approximately 15 dB to 25 dB. It is worth noting that the COP of the direct-link scheme becomes higher than that of the than that of the no-direct-link scheme in the medium-to-high SNR region. This counterintuitive result varies because the direct BS-D_i link experiences severe path loss and thus contributes only a weak signal component. When this weak direct signal is combined with the IRS-reflected signal, the two compo-

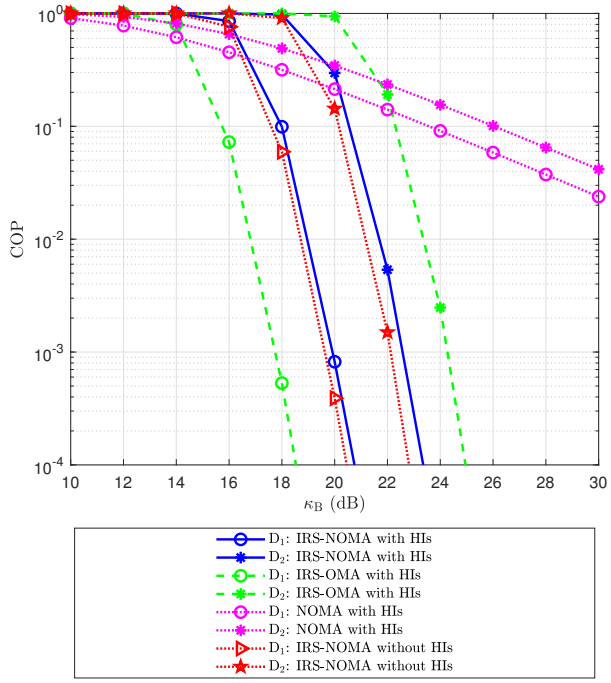

Fig. 11: Comparison of the COP for D_i versus κ_B, and baselines under identical conditions: IRS-NOMA with HIs, OMA with IRS, NOMA without IRS, and IRS-NOMA without HIs.

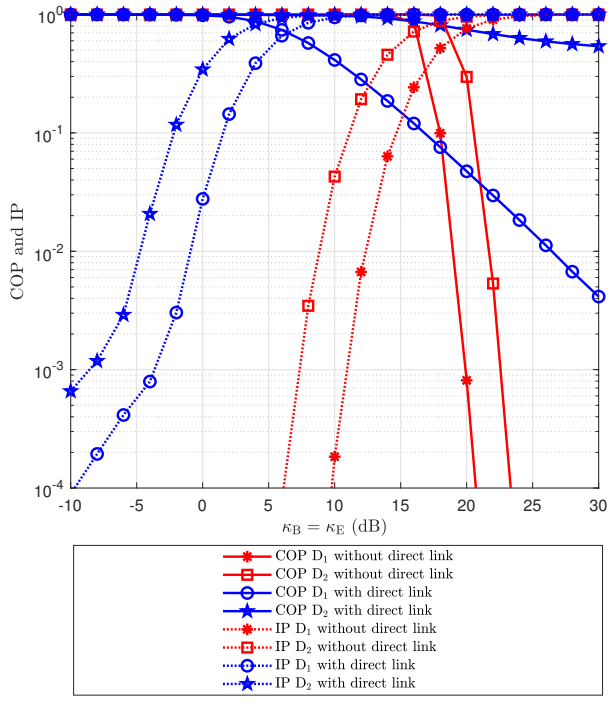

Fig. 12: Trade-off the COP and IP of D_1 and D_2 versus κ_B for the direct-link scheme and no-direct-link schemes.

nents may suffer from imperfect phase alignment, leading to partial or even destructive interference. Moreover, since the IRS is optimized primarily for the reflected path, the presence of a non-optimized direct link can degrade a higher COP compared to the no-direct-link case, where the IRS-reflected path is fully exploited without interference from the direct component. However, the IP performance of D_i exhibits the opposite behavior; due to the inherent trade-off, the direct-link scheme results in a higher IP compared to the no-direct-link scheme.

The analytical and simulation results provide several insights for designing a practical IRS-assisted NOMA system. First, the characterization of the COP and IP across different SNR regimes helps determine the reliable operating conditions required to achieve a target performance level. Second, the sensitivity analysis with respect to HIs suggests that system designers should prioritize high-quality components at the BS, whereas low-cost hardware can be tolerated at the users. Third, the comparison between the analytical expressions and the DNN-based predictions demonstrates that learning-based methods can be used to reduce computational complexity in dynamic environments. Moreover, our findings align with recent proof-of-concept prototypes reported in the literature [40,41], where IRSs equipped with approximately 160 reflectors were designed, fabricated, and experimentally validated. These prototypes demonstrated that IRS technology can effectively mitigate loss and extend coverage in real-world wireless communications. Collectively, these observations bridge our theoretical results with practical design considerations for future IRS-enabled networks. Moreover, these observations bridge our theoretical results with considerations for future IRS-enabled networks and highlight the usefulness of the derived analytical expressions for performance optimization.

8. Conclusion

In this article, we investigated the performance and security of a downlink secure network integrating NOMA and IRS techniques. Moreover, we considered a scenario where the BS transmits signals via an IRS to legitimate users, while multiple Es attempt interception. We derived closed-form expressions for the system's COP and IP, and further validated them using DNNs for predictive analysis. Our results highlight the impact of IRS element numbers, reflection coefficients, HIs, number of Es, and the power allocation on system performance and security. This study demonstrates how combining analytical derivations with DNN-based predictions can provide a comprehensive understanding of IRS-NOMA system performance and security,

offering a benchmark for future research. Beyond its theoretical contributions, the presented analysis can serve as a design reference for practical secure wireless applications, such as secure IoT deployments and mission-critical industrial networks, where both reliability and PLS are required.In addition, this work still contains several limitations that open promising directions for future research. The analysis relies on perfect CSI and continuous IRS phase shifts, whereas practical IRS implementations often suffer from CSI uncertainty and quantized phase control. Moreover, potential IRS-E leakage and model mismatches were not fully accounted for in the main framework. In the future, extending the system design to incorporate imperfect CSI, phase quantization, and more realistic IRS leakage characteristics represents an important direction to further enhance the practicality of IRS-assisted NOMA systems. Future work will extend the analysis to non-i.i.d. E channels, such as correlated or heterogeneous channel conditions, to evaluate the performance and robustness of the proposed IRS-NOMA schemes under more realistic scenarios. The presented analytical and learning-based framework can serve as a useful benchmark for future studies on secure IRS-assisted NOMA systems and may facilitate the development of adaptive and real-time resource allocation strategies in beyond-5G/6G networks.

Author Contributions

Both P. T. T. and M.-S. V. N. carried out analytical computations and numerical simulations. Q.-A. B. and L. V. T. wrote the whole paper. While T. T. D., P. T. T., and M.-S. V. N. developed the system model and proposed the idea. Finally, Q.-A. B. supervises this work. All authors contributed to the final version of the manuscript.

Acknowledgment

This research is funded by Ton Duc Thang University under grant number FOSTECT.2025.23.

References

[1] MEAD, J. A., et al. Secure RIS-Aided FD NOMA Communications for Hardware Impaired IoT Networks. *IEEE Internet of Things Journal*. 2025, vol. 12, no. 14, pp. 28332-28347. DOI: 10.1109/JIOT.2025.3566504.

[2] MINH TRAN, et al. Outage Analysis of a Hybrid Relay-Backscatter Communication System with Energy Harvesting for IoT and 6G Networks. *IEEE Access*. 2025, vol. 13, pp. 188605-188617. DOI: 10.1109/ACCESS.2025.3628053.

[3] HUNG, T. C., et al. Performance Analysis of Ergodic Rate and Effective Capacity for RIS-Assisted NOMA Networks Over Nakagamim Fading Environments. *IEEE Access*. 2024, vol. 12, pp. 181271-181281. DOI: 10.1109/ACCESS.2024.3509856.

[4] BUI, V. M., et al. Precise Analysis of Secrecy Outage Probability and Eavesdropping Strategies in Secure, Energy-Efficient Wireless Networks for Copyright Protection of Digital Contents. *IEEE Access*. 2025, vol. 13, pp. 148495-148509. DOI: 10.1109/ACCESS.2025.3601007.

[5] NGUYEN, T. N, et al. Security and Reliability Analysis of Satellite-Terrestrial Multi-Relay Networks with Imperfect CSI. *IEEE Systems Journal*. 2023, vol. 17, no. 2, pp. 2824-2835. DOI: 10.1109/JSYST.2022.3201128.

[6] PALA, S., et al. Secure RIS-Assisted Hybrid Beamforming Design With Low-Resolution Phase Shifters. *IEEE Transactions on Wireless Communications*. 2024, vol. 23, no. 8, pp. 10198-10212. DOI: 10.1109/TWC.2024.3370372.

[7] QUANG, P. M., et al. Performance Evaluation Of Reconfigurable Intelligent Surface Aided Multi-Hop Relaying Schemes With Short Packet Communication. *Advances in Electrical and Electronic Engineering*. 2024, vol. 22, no. 1, pp. 96-105. DOI: 10.15598/aeee.v22i1.5583.

[8] SANG, N. Q., et al. Outage Performance Analysis of STAR-RIS-NOMA Networks under Imperfect CSI. *Advances in Electrical and Electronic Engineering*. 2024, vol. 22, no. 3, pp. 260-270. DOI: 10.15598/aeee.v22i3.5546.

[9] GUO, S., S. LV, H. ZHANG, J. YE, P. ZHANG. Reflecting modulation. *IEEE Journal on Selected Areas in Communications*. 2020, vol. 38, no. 11, pp. 2548–2561. DOI: 10.1109/JSAC.2020.3007060.

[10] PHU, L. S., T. N. NGUYEN, B. V. MINH, P. T. TIN, M. VOZNAK. Enhancing short-packet communications: BLER performance in RIS-assisted ambient backscatter NOMA systems. *PLoS One* . 2025, vol. 20, no. 8. DOI: 10.1371/journal.pone.0328545.

[11] VU, T.-H., T. N. NGUYEN, T.-T. NGUYEN, S. KIM. Hybrid Active-Passive STAR-RIS-Based NOMA Systems: Energy/Rate-Reliability Trade-Offs and Rate Adaptation. *IEEE Wireless Communications Letters*. 2025, vol. 14, no. 1, pp. 238-242. DOI: 10.1109/LWC.2024.3497978.

[12] PEI, Y., et al. Secrecy Outage Probability Analysis for Downlink RIS-NOMA Networks With On-Off Control. *IEEE Transactions on Vehicular Technology*. 2023, vol. 72, no. 9, pp. 11772-11786. DOI: 10.1109/TVT.2023.3267531.

[13] LE, S.-P., et al. On the Secrecy Performance of Reconfigurable Intelligent Surfaces-Assisted Satellite Networks Under Shadow-Rician Channels. *IEEE Transactions on Aerospace and Electronic Systems*. 2025, vol. 61, no. 3, pp. 6794-6808. DOI: 10.1109/TAES.2025.3532227.

[14] LE, A.-T., T.-H. VU, T. N. NGUYEN, B. V. MINH, M. VOZNAK. On Performance of Cooperative Satellite-AAV-Secured Reconfigurable Intelligent Surface Systems With Phase Errors. *IEEE Communications Letters*. 2025, vol. 29, no. 4, pp. 799-803. DOI: 10.1109/LCOMM.2025.3543732.

[15] LI, X., et al. Covert Communications With Enhanced Physical Layer Security in RIS-Assisted Cooperative Networks. *IEEE Transactions on Wireless Communications*. 2025, vol. 24, no. 7, pp. 5605-5619. DOI: 10.1109/TWC.2025.3548024.

[16] SANG, N. Q., et al. Performance of RIS-Secured Short-Packet NOMA Systems with Discrete Phase-Shifter to Protect Digital Content and Copyright Against Untrusted User. *IEEE Access*. 2025, vol. 13, pp. 21580-21593. DOI: 10.1109/ACCESS.2025.3535813.

[17] LIU, H., J. LUO, S. WANG, H. DING. Effective Secrecy Capacity for RIS-Assisted NOMA Communication Networks. *IEEE Transactions on Vehicular Technology*. 2025, vol. 74, no. 1, pp. 1379-1384. DOI: 10.1109/TVT.2024.3456903.

[18] ZHOUU, G., et al. Secure Wireless Communication in RIS-Aided MISO System With Hardware Impairments. *IEEE Wireless Communications Letters*. 2021, vol. 10, no. 6, pp. 1309-1313. DOI: 10.1109/LWC.2021.3064992.

[19] ZHANG, Q., et al. Robust Beamforming Design for RIS-Aided NOMA Secure Networks with Transceiver Hardware Impairments. *IEEE Transactions on Communications*. 2023, vol. 71, no. 6, pp. 3637-3649. DOI: 10.1109/TCOMM.2023.3251345.

[20] PENG, Z., et al. Robust Transmission Design for RIS-Assisted Secure Multiuser Communication Systems in the Presence of Hardware Impairments. *IEEE Transactions on Wireless Communications*. 2023, vol. 22, no. 11, pp. 7506-7521. DOI: 10.1109/TWC.2023.3252046.

[21] VU, T. -H., T. -V. NGUYEN, D. B. DA COSTA, S. KIM. Performance Analysis and Deep Learning Design of Underlay Cognitive NOMA-Based CDRT Networks With Imperfect SIC and Co-Channel Interference. *IEEE Transactions on Communications*. 2021, vol. 69, no. 12, pp. 8159-8174. DOI: 10.1109/TCOMM.2021.3110209.

[22] TAN, N. N., et al. Cooperative Satellite-Terrestrial Networks with Imperfect CSI and Multiple Jammers: Performance Analysis and Deep Learning Evaluation. *IEEE Systems Journal*. 2024, vol. 18, no.4, pp. 2062-2073. DOI: 10.1109/JSYST.2024.3463715.

[23] TIN, P. T., et al. System Modeling and Deep Learning-Based Security Analysis of Uplink NOMA Relay Networks with IRS and Fountain Codes. *Computer Modeling in Engineering & Sciences*. 2025, vol. 144, no. 2, pp. 2521–2543. DOI: 10.32604/cmes.2025.066669.

[24] UÇAR-GÜL, M., M. NAMDAR, O. ERGUL. RIS-Assisted NOMA Systems: Performance Analysis Under HWI and Channel Estimation Error. *IEEE Access*. 2025, vol. 13, pp. 127637-127649. DOI: 10.1109/ACCESS.2025.3590655.

[25] LIU, Z., et al. Exploiting the Direct Link in IRS Assisted NOMA Networks with Hardware Impairments. *Computer Modeling in Engineering & Sciences*. 2023, vol. 136, no. 1, pp. 767–785. DOI: 10.32604/cmes.2023.025300.

[26] MINH, B. V., et al. Precise Analysis of Secrecy Outage Probability and Eavesdropping Strategies in Secure, Energy-Efficient Wireless Networks for Copyright Protection of Digital Contents. *IEEE Access*. 2025, vol. 13, pp. 148495-148509. DOI: 10.1109/ACCESS.2025.3601007.

[27] LI, X., et al. Reliability and Security of CR-STAR-RIS-NOMA-Assisted IoT Networks. *IEEE Internet of Things Journal*. 2024, vol. 11, no. 17, pp. 27969-27980. DOI: 10.1109/JIOT.2023.3340371.

[28] CHENG, Y., et al. Downlink and Uplink Intelligent Reflecting Surface Aided Networks: NOMA and OMA. *IEEE Transactions on Wireless Communications*. 2021, vol. 20, no. 6, pp. 3988-4000. DOI: 10.1109/TWC.2021.3054841.

[29] YANG, L., et al. Secrecy Performance Analysis of RIS-Aided Wireless Communication Systems. *IEEE Transactions on Vehicular Technology*. 2020. vol. 69, no. 10, pp. 12296-12300. DOI: 10.1109/TVT.2020.3007521.

[30] YUE, X., et al. Simultaneously Transmitting and Reflecting Reconfigurable Intelligent Surface Assisted NOMA Networks. *IEEE Transactions on Wireless Communications*. 2023, vol. 22, no. 1, pp. 189-204. DOI: 10.1109/TWC.2022.3192211.

[31] YUE, X., et al. Exploiting Active RIS in NOMA Networks With Hardware Impairments. *IEEE Transactions on Vehicular Technology*. 2024, vol. 73, no. 6, pp. 8207-8221. DOI: 10.1109/TVT.2024.3352813.

[32] MINH, B. V., T. H. Q. MINH, V. D. Phan, H. T. NGUYEN. D2D Communication Network with the Assistance of Power Beacon under the Impact of Co-channel Interferences and Eavesdropper: Performance Analysis. *Advances in Electrical and Electronic Engineering*. 2023, vol. 21, no. 4, pp. 351-359. DOI: 10.15598/aeee.v21i4.5495.

[33] LE, A.-T., et al. Active-Reconfigurable-Repeater-Assisted NOMA Networks in Internet of Things: Reliability, Security, and Covertness. *IEEE Internet of Things Journal*. 2025, vol. 12, no. 7, pp. 8759-8772. DOI: 10.1109/JIOT.2024.3503278.

[34] LE, A. -T., T.-H. VU, T. N. NGUYEN, T.-L. TIEN, M. VOZNAK. Partial Multiplexing Power-Frequency Multiple Access for Active STAR-RIS Systems: Outage and Ergodic Perspectives. *IEEE Wireless Communications Letters*. 2025, vol. 14, no. 3, pp. 786-790. DOI: 10.1109/LWC.2024.3523387.

[35] LE, A.-T., et al. Physical layer security analysis for RIS-aided NOMA systems with non-colluding eavesdroppers. *Computer Communications*. 2024, vol. 219, pp. 194-203. DOI: 10.1016/j.comcom.2024.03.011.

[36] SHIM, K., T. N. DO, T.-V. NGUYEN, D. B. d. COSTA, B. AN. Enhancing PHY-Security of FD-Enabled NOMA Systems Using Jamming and User Selection: Performance Analysis and DNN Evaluation. *IEEE Internet of Things Journal*. 2021, vol. 8, no. 24, pp. 17476-17494. DOI: 10.1109/JIOT.2021.3080425.

[37] TAN, N.N., et al. Performance Evaluation of User Selection Protocols in Random Networks with Energy Harvesting and Hardware Impairments. *Advances in Electrical and Electronic Engineering*. 2016, vol. 14, no. 4, pp. 372-377. DOI: 10.15598/aeee.v14i4.1783.

[38] ANH, T. L., et al. Power Beacon and NOMA-Assisted Cooperative IoT Networks with Co-Channel Interference: Performance Analysis and Deep Learning Evaluation. *IEEE Transactions on Mobile Computing*. 2024, vol. 23, no. 6, pp. 7270-7283. DOI: 10.1109/TMC.2023.3333764.

[39] HEMA, P. P., A. V. BABU. Power Adaptation for Optimizing Secrecy Energy Efficiency in NOMA-Enabled Underlay Cognitive Radio Networks and DNN-Based Evaluation. *IEEE Open Journal of the Communications Society*. 2025, vol. 6, pp. 820-839. DOI: 10.1109/OJCOMS.2025.3527510.

[40] ARAGHI, A., et al. Reconfigurable Intelligent Surface (RIS) in the Sub-6 GHz Band: Design, Implementation, and Real-World Demonstration. *IEEE Access*. 2022, vol. 10, pp. 2646-2655. DOI: 10.1109/ACCESS.2022.3140278.

[41] TRICHOPOULOS, G. C., et al. Design and Evaluation of Reconfigurable Intelligent Surfaces in Real-World Environment. *IEEE Open Journal of the Communications Society*. 2022, vol. 3, pp. 462-474. DOI: 10.1109/OJCOMS.2022.3158310.

[42] ANNAMALAI, A., C. TELLAMBURA, J. MATYJAS. A New Twist on the Generalized Marcum Q-Function QM(a, b) with Fractional-Order M and Its Applications. 6th IEEE Consumer Communications and Networking Conference, Las Vegas, NV, USA. 2009, pp. 1-5. DOI: 10.1109/CCNC.2009.4784840.

[43] GRADSHTEYN, I. S., I. M. RYZHIK. Table of Integrals, Series, and Products. *7th ed. San Diego, CA, USA: Academic*. 2007.

Appendix A

Based on (2), (3) and (9), $\mathrm{COP}_{\mathrm{D}_1}$ can be reformulated as (30) (shown at the top of the next page).

Next, in the BS-IRS-D_i link, our objective is to optimize the channel quality for D_i by fine-tuning the IRS parameters. This involves maximizing $|\mathbf{g}_{\mathrm{I}}\mathbf{\Phi}_i\mathbf{g}_{\mathrm{d}_i}| = \left|\sum_{s=1}^{S_i}\chi_s g_{\mathrm{I},s}g_{\mathrm{d}_i,s}e^{j\omega_s}\right|$ [28], where $g_{\mathrm{I},s}$ and $g_{\mathrm{d}_i,s}$ denote the s-th elements of $\mathbf{g}_{\mathrm{I}}$ and $\mathbf{g}_{\mathrm{d}_i}$, respectively. This can be achieved by intelligently adjusting the phase-shift variable ω_s for each element while ensuring that all $g_{\mathrm{I},s}g_{\mathrm{d}_i,s}e^{j\omega_s}$ are set to be the same. As a result, there is not only one solution for $\{\omega_s\}, (s = 1, \ldots, S_i)$; instead, the generalized solution is given by $\omega_s = \overline{\omega} - \arg\left(g_{\mathrm{I},s}g_{\mathrm{d}_i,s}\right)$ with $\overline{\omega}$ sis an arbitrary constant ranging in $[0, 2\pi)$. Upon implementing the optimal $\{\omega_s\}$, we obtain [28]:

$$|\mathbf{g}_{\mathrm{I}}\mathbf{\Phi}_i\mathbf{g}_{\mathrm{d}_i}|^2 = \chi^2\left(\sum_{s=1}^{S_i}|g_{\mathrm{I},s}|\,|g_{\mathrm{d}_i,s}|\right)^2, \tag{31}$$

where we assume the conditions $\chi_s = \chi$ and $\forall_s$ without any loss of generality [28].

Based on the Appendix I in [28], the cumulative distribution function (CDF) and probability density function (PDF) of BS-IRS-D_i link channels are ascertained

$$\begin{aligned}\mathrm{COP}_{\mathrm{D}_1} =& 1-\Pr\left(\frac{|\mathbf{g}_{\mathrm{I}}\mathbf{\Phi}_1\mathbf{g}_{\mathrm{d}_1}|^2 d_{\mathrm{BI}}^{-\lambda} d_{\mathrm{ID}_1}^{-\lambda}\rho_2\kappa_{\mathrm{B}}}{|\mathbf{g}_{\mathrm{I}}\mathbf{\Phi}_1\mathbf{g}_{\mathrm{d}_1}|^2\varepsilon_1\kappa_{\mathrm{B}}+1}\geq\nu_2, \frac{|\mathbf{g}_{\mathrm{I}}\mathbf{\Phi}_1\mathbf{g}_{\mathrm{d}_1}|^2 d_{\mathrm{BI}}^{-\lambda} d_{\mathrm{ID}_1}^{-\lambda}\rho_1\kappa_{\mathrm{B}}}{|\mathbf{g}_{\mathrm{I}}\mathbf{\Phi}_1\mathbf{g}_{\mathrm{d}_1}|^2\varepsilon_2\kappa_{\mathrm{B}}+1}\geq\nu_1\right)\\ =& 1-\Pr\left[|\mathbf{g}_{\mathrm{I}}\mathbf{\Phi}_1\mathbf{g}_{\mathrm{d}_1}|^2\geq\frac{\nu_2}{\kappa_{\mathrm{B}}\left(d_{\mathrm{BI}}^{-\lambda}d_{\mathrm{ID}_1}^{-\lambda}\rho_2-\nu_2\varepsilon_1\right)}, |\mathbf{g}_{\mathrm{I}}\mathbf{\Phi}_1\mathbf{g}_{\mathrm{d}_1}|^2\geq\frac{\nu_1}{\kappa_{\mathrm{B}}\left(d_{\mathrm{BI}}^{-\lambda}d_{\mathrm{ID}_1}^{-\lambda}\rho_1-\nu_1\varepsilon_2\right)}\right]\\ =& 1-\Pr\left[|\mathbf{g}_{\mathrm{I}}\mathbf{\Phi}_1\mathbf{g}_{\mathrm{d}_1}|^2\geq\max\left(\frac{\nu_2}{\kappa_{\mathrm{B}}\left(d_{\mathrm{BI}}^{-\lambda}d_{\mathrm{ID}_1}^{-\lambda}\rho_2-\nu_2\varepsilon_1\right)}, \frac{\nu_1}{\kappa_{\mathrm{B}}\left(d_{\mathrm{BI}}^{-\lambda}d_{\mathrm{ID}_1}^{-\lambda}\rho_1-\nu_1\varepsilon_2\right)}\right)\right].\end{aligned} \tag{30}$$

by

$$\begin{aligned}F_{H_i}(w) =& 1-Q_{1/2}\left(\sqrt{\eta_{H_i}}, \sqrt{w}\right)\\ \overset{(m)}{=}& \exp\left(-\frac{\eta_{H_i}}{2}\right)\sum_{c=0}^{\infty}\frac{\eta_{H_i}^c\gamma\left(c+1/2, w/2\right)}{c!2^c\Gamma\left(c+1/2\right)},\end{aligned} \tag{32}$$

and

$$\begin{aligned}f_{H_i}(w) =& \frac{\eta_{H_i}^{1/4}}{2}\exp\left(-\frac{w+\eta_{H_i}}{2}\right)\eta_{H_i}^{1/4}I_{-1/2}\left(\sqrt{\eta_{H_i}w}\right)\\ \overset{(n)}{=}& \exp\left(-\frac{w+\eta_{H_i}}{2}\right)\sum_{c=0}^{\infty}\frac{\eta_{H_i}^c w^{c-1/2}}{c!2^{2c+1/2}\Gamma\left(c+1/2\right)}.\end{aligned} \tag{33}$$

where (m) and (n) are acquired from [42, eq. (18)] and [43, eq. (8.445)], respectively. $H_i = \frac{\left(\sum_{s=1}^{S_i}|g_{\mathrm{I},s}||g_{\mathrm{d}_{i,s}}|\right)^2}{d(1-\sigma_i)}$, $\eta_{H_i} = \frac{S_i\sigma_i}{1-\sigma_i}$, $\sigma_i = \frac{1}{m_{g_{\mathrm{I},s}}m_{g_{\mathrm{d}_{i,s}}}}\left[\frac{\Gamma\left(m_{g_{\mathrm{I},s}}+1/2\right)}{\Gamma\left(m_{g_{\mathrm{I},s}}\right)}\right]^2\left[\frac{\Gamma\left(m_{g_{\mathrm{d}_{i,s}}}+1/2\right)}{\Gamma\left(m_{g_{\mathrm{d}_{i,s}}}\right)}\right]^2$ [28]. In scenarios where the number of reflecting elements, denoted as S, is large, the variable H_i typically adheres to a noncentral chi-square distribution characterized by $H_i \sim H_i^2(\eta_{H_i})$. The function $I_x(.)$ represents the modified Bessel function of the first kind. Additionally, $Q_x(.)$ denotes the Marcum Q-function, while $\Gamma(.)$ signifies the gamma function. Furthermore, $\gamma(.,.)$ corresponds to the lower incomplete gamma function.

From (30), and subject to the condition $d_{\mathrm{BI}}^{-\lambda}d_{\mathrm{ID}_1}^{-\lambda}\rho_2 > \nu_2\varepsilon_1$ and $d_{\mathrm{BI}}^{-\lambda}d_{\mathrm{ID}_1}^{-\lambda}\rho_1 > \nu_1\varepsilon_2$. $\mathrm{COP}_{\mathrm{D}_1}$ can be expressed as (34), where $\Xi = \max\left[\frac{\nu_2}{\kappa_{\mathrm{B}}\left(d_{\mathrm{BI}}^{-\lambda}d_{\mathrm{ID}_1}^{-\lambda}\rho_2-\nu_2\varepsilon_1\right)}, \frac{\nu_1}{\kappa_{\mathrm{B}}\left(d_{\mathrm{BI}}^{-\lambda}d_{\mathrm{ID}_1}^{-\lambda}\rho_1-\nu_1\varepsilon_2\right)}\right]$.

Based on the CDF function from equation (32), $\mathrm{COP}_{\mathrm{D}_1}$ can be calculated as

$$\mathrm{COP}_{\mathrm{D}_1} = \exp\left(-\frac{\eta_{H_1}}{2}\right)\sum_{c=0}^{\infty}\frac{\eta_{H_1}^c\gamma\left(c+\frac{1}{2}, \frac{\Xi S_1(1-\sigma_1)}{2\chi^2}\right)}{c!2^c\Gamma\left(c+\frac{1}{2}\right)}. \tag{35}$$

The proof is done.

Appendix B

Based on (5) and (11), $\mathrm{COP}_{\mathrm{D}_2}$ can be expressed as (36), shown at the top of the next page.

Based on the CDF function from (32), and subject to the condition $\rho_2 > \nu_2\varepsilon_3$ and $\sigma_2 < 1$. $\mathrm{COP}_{\mathrm{D}_2}$ is calculated as

$$\begin{aligned}\mathrm{COP}_{\mathrm{D}_2} =& \exp\left(-\frac{\eta_{H_2}}{2}\right)\\ &\times\sum_{c=0}^{\infty}\frac{\eta_{H_2}^c\gamma\left(c+\frac{1}{2}, \frac{\nu_2 S_2(1-\sigma_2)}{2\chi^2\kappa_B\left(d_{\mathrm{BI}}^{-\lambda}d_{\mathrm{ID}_2}^{-\lambda}\rho_2-\nu_2\varepsilon_3\right)}\right)}{c!2^c\Gamma\left(c+\frac{1}{2}\right)}.\end{aligned} \tag{37}$$

The proof is done.

Appendix C

Based on (8) and (13), $\mathrm{IP}_{\mathrm{D}_1}$ can be reformulated as

$$\begin{aligned}\mathrm{IP}_{\mathrm{D}_1} =& \Pr\left(\gamma_{\mathrm{E}_u}^{v_1}\geq\nu_1\right) = \Pr\left(\frac{\tau_{\mathrm{BE}}d_{\mathrm{E}_u}^{-\lambda}\rho_1\kappa_{\mathrm{E}}}{\tau_{\mathrm{BE}}d_{\mathrm{E}_u}^{-\lambda}\varepsilon_5\kappa_{\mathrm{E}}+1}\geq\nu_1\right)\\ =& \Pr\left[\tau_{\mathrm{BE}}d_{\mathrm{E}_u}^{-\lambda}\kappa_{\mathrm{E}}\left(\rho_1-\nu_1\varepsilon_5\right)\geq\nu_1\right]\\ =& \Pr\left[\tau_{\mathrm{BE}}\geq\frac{\nu_1}{d_{\mathrm{E}_u}^{-\lambda}\kappa_{\mathrm{E}}\left(\rho_1-\nu_1\varepsilon_5\right)}\right].\end{aligned} \tag{38}$$

Next, let us examine two sets of independent and identically distributed (i.i.d.) exponential random variables, denoted as $|g_{\mathrm{E}_u}|^2, (u\in\{1,\ldots,U\})$, characterized by the parameters $\mu_{g_{\mathrm{E}_u}}$. The CDF and PDF for the maximum value of these random variables $\tau_{\mathrm{BE}} = \max\left(|g_{\mathrm{E}_1}|^2, |g_{\mathrm{E}_2}|^2, \ldots, |g_{\mathrm{E}_U}|^2\right)$ can be articulated as [26]

$$\begin{aligned}F_{\tau_{\mathrm{BE}}}(w) =& 1-\sum_{b=1}^{U}\binom{U}{b}(-1)^{b-1}\\ &\times\exp\left(-\frac{bw}{\mu_{g_{\mathrm{E}_u}}}\right),\end{aligned} \tag{39}$$

$$\begin{aligned}\mathrm{COP}_{\mathrm{D}_1} =& 1-\Pr\left[\frac{\chi^2\left(\sum\limits_{s=1}^{S_1}\left|g_{\mathrm{I},s}\right|\left|g_{\mathrm{d}_{1,s}}\right|\right)^2}{S_1\left(1-\sigma_1\right)}\geq\Xi\right]=1-\Pr\left[\left(\sum_{s=1}^{S_1}\left|g_{\mathrm{I},s}\right|\left|g_{\mathrm{d}_{1,s}}\right|\right)^2\geq\frac{\Xi S_1\left(1-\sigma_1\right)}{\chi^2}\right]\\ =&1-\left[1-F_{\left(\sum\limits_{s=1}^{S_1}\left|g_{\mathrm{I},s}\right|\left|g_{\mathrm{d}_{1,s}}\right|\right)^2}\left(\frac{\Xi S_1\left(1-\sigma_1\right)}{\chi^2}\right)\right]=F_{\left(\sum\limits_{s=1}^{S_1}\left|g_{\mathrm{I},s}\right|\left|g_{\mathrm{d}_{1,s}}\right|\right)^2}\left(\frac{\Xi S_1\left(1-\sigma_1\right)}{\chi^2}\right).\end{aligned}\tag{34}$$

$$\begin{aligned}&\mathrm{COP}_{\mathrm{D}_2}=1-\Pr\left(\gamma_{\mathrm{D}_2}^{v_2}\geq\nu_2\right)=1-\Pr\left(\frac{\left|\mathbf{g}_{\mathrm{I}}\boldsymbol{\Phi}_2\mathbf{g}_{\mathrm{d}_2}\right|^2 d_{\mathrm{BI}}^{-\lambda}d_{\mathrm{ID}_2}^{-\lambda}\rho_2\kappa_{\mathrm{B}}}{\left|\mathbf{g}_{\mathrm{I}}\boldsymbol{\Phi}_2\mathbf{g}_{\mathrm{d}_2}\right|^2 d_{\mathrm{BI}}^{-\lambda}d_{\mathrm{ID}_2}^{-\lambda}\varepsilon_3\kappa_{\mathrm{B}}+1}\geq\nu_2\right)\\ &=1-\Pr\left[\left|\mathbf{g}_{\mathrm{I}}\boldsymbol{\Phi}_2\mathbf{g}_{\mathrm{d}_2}\right|^2\geq\frac{\nu_2}{d_{\mathrm{BI}}^{-\lambda}d_{\mathrm{ID}_2}^{-\lambda}\kappa_{\mathrm{B}}\left(\rho_2-\nu_2\varepsilon_3\right)}\right]=1-\Pr\left[\frac{\chi^2\left(\sum\limits_{s=1}^{S_2}\left|g_{\mathrm{I},s}\right|\left|g_{\mathrm{d}_{2,s}}\right|\right)^2}{S_2\left(1-\sigma_2\right)}\geq\frac{\nu_2}{d_{\mathrm{BI}}^{-\lambda}d_{\mathrm{ID}_2}^{-\lambda}\kappa_{\mathrm{B}}\left(\rho_2-\nu_2\varepsilon_3\right)}\right]\\ &=1-\Pr\left[\left(\sum_{s=1}^{S_2}\left|g_{\mathrm{I},s}\right|\left|g_{\mathrm{d}_{2,s}}\right|\right)^2\geq\frac{\nu_2 S_2\left(1-\sigma_2\right)}{\chi^2 d_{\mathrm{BI}}^{-\lambda}d_{\mathrm{ID}_2}^{-\lambda}\kappa_{\mathrm{B}}\left(\rho_2-\nu_2\varepsilon_3\right)}\right]\\ &=1-\left[1-F_{\left(\sum\limits_{s=1}^{S_2}\left|g_{\mathrm{I},s}\right|\left|g_{\mathrm{d}_{2,s}}\right|\right)^2}\left(\frac{\nu_2 S_2\left(1-\sigma_2\right)}{\chi^2 d_{\mathrm{BI}}^{-\lambda}d_{\mathrm{ID}_2}^{-\lambda}\kappa_{\mathrm{B}}\left(\rho_2-\nu_2\varepsilon_3\right)}\right)\right]=F_{\left(\sum\limits_{s=1}^{S_2}\left|g_{\mathrm{I},s}\right|\left|g_{\mathrm{d}_{2,s}}\right|\right)^2}\left(\frac{\nu_2 S_2\left(1-\sigma_2\right)}{\chi^2 d_{\mathrm{BI}}^{-\lambda}d_{\mathrm{ID}_2}^{-\lambda}\kappa_{\mathrm{B}}\left(\rho_2-\nu_2\varepsilon_3\right)}\right).\end{aligned}\tag{36}$$

and

$$\begin{aligned}f_{\tau_{\mathrm{BE}}}\left(w\right)=&\sum_{b=1}^{U}\binom{U}{b}\left(-1\right)^{b-1}\frac{b}{\mu_{g_{\mathrm{E}_u}}}\\ &\times\exp\left(-\frac{bw}{\mu_{g_{\mathrm{E}_u}}}\right).\end{aligned}\tag{40}$$

Continuing, based on the CDF function from (39), and subject to the condition $\rho_1>\nu_1\varepsilon_5$. $\mathrm{IP}_{\mathrm{D}_1}$ is subsequently calculated as follows

$$\begin{aligned}\mathrm{IP}_{\mathrm{D}_1}=&1-F_{\tau_{\mathrm{BE}}}\left(\frac{\nu_1}{\kappa_{\mathrm{E}}\left(d_{\mathrm{E}_u}^{-\lambda}\rho_1-\nu_1\varepsilon_5\right)}\right)\\ =&\sum_{b=1}^{U}\binom{U}{b}\left(-1\right)^{b-1}\\ &\times\exp\left[-\frac{b\nu_1}{\kappa_{\mathrm{E}}\mu_{g_{\mathrm{E}_u}}\left(d_{\mathrm{E}_u}^{-\lambda}\rho_1-\nu_1\varepsilon_5\right)}\right].\end{aligned}\tag{41}$$

The proof is done.

Appendix D

Based on (7) and (15), the formulation of $\mathrm{IP}_{\mathrm{D}_2}$ can be revised as follows

$$\begin{aligned}\mathrm{IP}_{\mathrm{D}_2}=&\Pr\left(\gamma_{\mathrm{E}_u}^{v_2}\geq\nu_2\right)\\ =&\Pr\left(\frac{\tau_{\mathrm{BE}}d_{\mathrm{E}_u}^{-\lambda}\rho_2\kappa_{\mathrm{E}}}{\tau_{\mathrm{BE}}d_{\mathrm{E}_u}^{-\lambda}\varepsilon_4\kappa_{\mathrm{E}}+1}\geq\nu_2\right)\\ =&\Pr\left[\tau_{\mathrm{BE}}d_{\mathrm{E}_u}^{-\lambda}\rho_2\kappa_{\mathrm{E}}\geq\nu_2\left(\tau_{\mathrm{BE}}d_{\mathrm{E}_u}^{-\lambda}\varepsilon_4\kappa_{\mathrm{E}}+1\right)\right]\\ =&\Pr\left[\tau_{\mathrm{BE}}d_{\mathrm{E}_u}^{-\lambda}\kappa_{\mathrm{E}}\left(\rho_2-\nu_2\varepsilon_4\right)\geq\nu_2\right]\\ =&\Pr\left[\tau_{\mathrm{BE}}\geq\frac{\nu_2}{d_{\mathrm{E}_u}^{-\lambda}\kappa_{\mathrm{E}}\left(\rho_2-\nu_2\varepsilon_4\right)}\right].\end{aligned}\tag{42}$$

Proceeding further, utilizing the CDF function derived from (39), and subject to the condition $\rho_2>\nu_2\varepsilon_4$. $\mathrm{IP}_{\mathrm{D}_2}$ can be calculated as

$$\begin{aligned}\mathrm{IP}_{\mathrm{D}_2}=&1-F_{\tau_{\mathrm{BE}}}\left(\frac{\nu_2}{\kappa_{\mathrm{E}}\left(d_{\mathrm{E}_u}^{-\lambda}\rho_2-\nu_2\varepsilon_4\right)}\right)\\ =&\sum_{b=1}^{U}\binom{U}{b}\left(-1\right)^{b-1}\\ &\times\exp\left[-\frac{b\nu_2}{\kappa_{\mathrm{E}}\mu_{g_{\mathrm{E}_u}}\left(d_{\mathrm{E}_u}^{-\lambda}\rho_2-\nu_2\varepsilon_4\right)}\right].\end{aligned}\tag{43}$$

The proof is done.

Appendix E

To implement the proposed prediction framework efficiently and consistently, we design a unified training and evaluation pipeline. The detailed procedure is presented in Algorithm 1 [36, 38].

Algorithm 1 Procedure for training and testing the DNN.

Require: DNN hyperparameters: H_{dn}, dn= 128, RMES threshold ($RMES_{th} = 10^{-2}$), learning rate $= 10^{-3}$

Ensure:

1: Split dataset into ∇_{tra}, ∇_{va}, ∇_{tes}
2: Construct a fully connected DNN with H_{dn} layer and dn
3: **repeat**
4: Train on ∇_{tra} and validate on ∇_{va}
5: Save validated model as `validatedDNN.h5`
6: Computer RMSE model as ∇_{tes}
7: **until** RMSE $<$ $RMSE_{th}$
8: Save final model as `validatedDNN.h5`
9: **return** `validatedDNN.h5`